A Thesis

entitled

Modeling of Concrete Anchors Supporting Non-Structural Components Subjected to

Strong Wind and Adverse Environmental Conditions

by

Sálvio Aragão Almeida Júnior

Submitted to the Graduate Faculty as partial fulfillment of the requirements for the

Master of Science Degree in

Civil Engineering

____
Dr. Serhan Guner, Committee Chair

____
Dr. Douglas Nims, Committee Member

____
Dr. Luis Mata, Committee Member

____
Dr. Cyndee Gruden, Dean
College of Graduate Studies

The University of Toledo

August 2019

An Abstract of

Modeling of Concrete Anchors Supporting Non-Structural Components Subjected to Strong Wind and Adverse Environmental Conditions

by

Sálvio Aragão Almeida Júnior

Submitted to the Graduate Faculty as partial fulfillment of the requirements for the Master of Science Degree in
Civil Engineering

The University of Toledo
August 2019

Hurricanes are responsible for approximately $28bn of damage every year in the United States, which is expected to increase to $151bn/year by the year 2075 due to climate change propelling more destructive hurricanes. Reconnaissance investigations estimate that 35% of this damage comes from anchorage failure of non-structural components (NSC). The design of NSC anchorage is traditionally done based on experimental results from quasi-static single-anchor tests, which neglect the dynamic effects of strong wind loading. During strong winds, the anchorage of NSCs can be damaged due to bending of the NSC-supporting beams, which has not yet been quantified. In addition, the adverse environmental conditions of elevated temperatures and concrete cracking to which these anchors are exposed prior to hurricane incidence contribute to the alarming anchor failure rates observed today. This study aims to investigate and quantify the damaging influence of the bending of the NSC-supporting beams and adverse environmental conditions on NSC anchorage to advance the current knowledge and propose new design recommendations to mitigate hurricane damage. To achieve this goal, 3D high-fidelity nonlinear finite element models ranging from single-anchors to holistic structures are

created to quantify the studied influences in the local- and system-level scales. The analyses indicate that the studied adverse environmental conditions reduce the anchor load capacity by up to 70%, while the bending of the NSC-supporting beams leads to a premature anchor failure up to 62% below its expected capacity. To avoid these premature failures, a safe-design region based on the geometry of the system is proposed. In addition, this study also aims to provide simpler and faster analysis alternatives to enable the usage of the proposed modeling technique by practitioner engineers. To achieve this goal: 1) a 2D modeling approach named "equivalent cone" is proposed and verified with the 3D numerical results; and 2) an artificial neural network is created, trained, and tested with experimental data from a worldwide database to rapidly predict the load capacity of anchors damaged by concrete cracking. These simpler alternatives significantly reduce the complexities involved in the anchor analysis while preserving the accuracy of the advanced 3D numerical models.

To the little padawan inside me that always wanted to be a master, to my family, and to Raphael Cardoso, my almost-brother.

Acknowledgments

Thank you to my advisor Dr. Serhan Guner for his orientation and opportunities provided, which were key in my academic and professional development. Thank you to the thesis committee, Dr. Douglas Nims and Dr. Luis Mata, for your guidance and feedback. Thank you to my research teammates for their valuable feedback, in special to Rafael Salgado for his continuous assistance since before the start of my graduate studies.

Thank you to professors A. Chowdhury for providing the wind load data that contributed to the research in Chapters 3 and 4 and R. Cook for providing the database on behalf of the ACI Committee 355 that contributed to the research in Chapter 6.

Thank you to my parents, Sálvio and Sandra Almeida, my brother Diego Almeida, and my family for their support and encouragement, which allowed me to pursue this education.

Thank you to my friends and beloved ones, who supported me throughout this journey. To Raphael Cardoso for keeping my passion for science alive and giving me a friendship no one else could. To Larissa Souza for giving me the purest love. To Joana Bitencourt for always dreaming with me and sharing existential crises. To Cayla Baldus for reminding me to always look up to the stars. To Stephanie Santana for being an inspiration and saying that I rock. To Gabriele Calixto for always talking to me. To Raísa Matos for believing in me. To Leonardo Araújo for the programming tips. To Thomas Maani for always offering me a place in his office. To Anusha Kadudula for buying me a guitar that helped maintain my mental health. To Vitor Rizzato and Eduardo Britto for the memes.

Table of Contents

List of Tables

List of Figures

List of Symbols

Δ ....Adhesive Displacement
ε_c................................Concrete Compressive Strain
ε_{cr}................................Concrete Cracking Strain
ε_p................................Concrete Compressive Strain at Peak Stress
ε_s................................Steel Strain
ε_{sh}................................Steel Hardening Initiation Strain
ε_t................................Concrete Tensile Strain
ε_u................................Steel Ultimate Strain
ε_y................................Steel Yield Strain
θ_{cr}................................Concrete Cracking Angle with the Horizontal
τ................................Static Adhesive Stress
τ_a................................Static Adhesive Strength
τ_{ad}................................Dynamic Adhesive Strength

A_{cone}................................Concrete Cone Cracking Surface Area
A_g................................Annular Gap
A_{trap}................................Concrete Trapezoidal Cracking Surface Area
B_{cone}................................Top of the Concrete Cone Cracking Area
b_{cr}................................Base of the Concrete Cracking Area
${}^{L}b_i$................................Bias of Neuron *i* in Layer *L*
B_{trap}................................Top of the Concrete Trapezoidal Cracking Area
d_a................................Anchor Rod Diameter
d_{hole}................................Anchor Borehole Diameter
d_{tip}................................Anchor Tip Diameter
E_{ANN}................................Total ANN Error
E_a................................Elastic Modulus of the Adhesive
E_c................................Elastic Modulus of the Concrete
ecc................................Eccentricity
E_s................................Elastic Modulus of the Steel
f_c................................Concrete Cylinder Compressive Stress
f'_c................................Concrete Cylinder Compressive Strength
f_s................................Static Steel Stress
f_t................................Static Concrete Tensile Stress
f'_t................................Static Concrete Tensile Strength
f'_{td}................................Dynamic Concrete Tensile Strength
f_u................................Steel Ultimate Stress

f_y ....Steel Yield Stress
h_{cone} ....Height of the Concrete Cone Cracking
h_{ef}................................Anchor Rod Embedment Depth
h_{tip}...............................Height of the Anchor Tip
h_{trap} ....Height of the Concrete Trapezoidal Cracking
${}^{L}n$ ....Number of Neurons in Layer *L*
P ....Anchor Load Capacity
S1,S2...........................Shear Forces on the NSC Anchorage
Temp...........................Temperature
t_{eq} ....Equivalent Concrete Thickness
T_i.................................Target Output for the Output Neuron *i*
t_{ini}................................Initial Concrete Thickness
t_w.................................W-Beam Web Thickness
V1,V2..........................Tension Forces on the NSC Anchorage
w_{cr}...............................Concrete Crack Width
${}^{L}w_{ij}$ ....Weight from Neuron *i* in Layer *L-1* to Neuron j in Layer *L*
${}^{L}x_i$...............................Input of Neuron *i* in Layer *L*
${}^{L}y_i$...............................Output of Neuron *i* in Layer *L*

Chapter 1

Introduction

Hurricanes are responsible for tens of billions of dollars in damage nearly every year in the United States (Masoomi et al., 2018). Since 1980 the U.S. has spent $928bn due to tropical storm damage (NOAA, 2019). Several studies suggest that this scenario is aggravated due to the urban development of coastal areas and increase in the destructiveness of hurricanes promoted by climate change (e.g. Guo, 2018; Dinan, 2017; Cui and Caracoglia, 2016; Liu, 2014; Michalski, 2014; Mudd et al., 2014; Emanuel, 2013; Knutson et al., 2013). According to Dinan (2017), the intensification of climate change is expected to increase the yearly hurricane damage cost from $28bn, in the year 2015, to $151bn (in 2015 monetary values) by the year 2075.

Examples of the intensification of windstorms have recently been felt in the United States during the uncommonly active hurricane season of 2017, which produced six major hurricanes, two of which reached the continental U.S. (NOAA, 2017). While this problem mostly affects the Atlantic and coastal states (e.g. Florida), areas far from the coast can be susceptible to strong winds too. A so-called “Bomb cyclone” recently affected the U.S. Midwest (Figure 1-1), promoting blizzards, flooding, and hurricane-like winds that exceed 36 m/s (80 m.p.h.) in areas as far as Nebraska (Cappucci and Samenow, 2019).

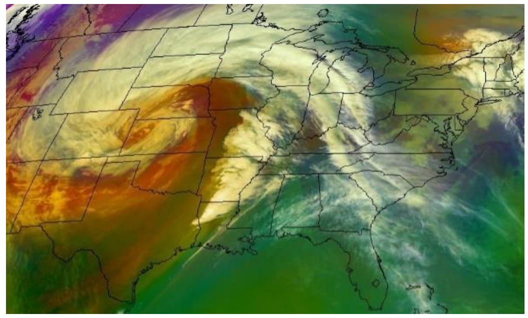

Figure 1-1: Satellite view of the “Bomb cyclone” (Cappucci and Samenow, 2019).

Nearly 35% of the post-storm repair cost is estimated to come from the repair of non-structural components (NSC), such as heating, ventilation, and air-conditioning (HVAC) systems; solar panels; and AC/DC inverters (Cope, 2004). NSCs are typically anchored to the rooftop of commercial buildings through steel anchors, where they stay for decades. However, they are often detached from the rooftop (Figure 1-2) when subjected to strong wind due to poor anchorage (FEMA, 2018; FEMA 2006). According to FEMA (2005), their detachment can result in:

- Roof openings, leading to water intrusion in the building.
- Interruption of operation of critical facilities (e.g. hospitals).
- Creation of high-momentum windborne debris.
- Damage to other structures.

Figure 1-2: Rooftop damage promoted by hurricane Irma in 2017 (Simon, 2017).

One factor promoting NSC anchorage failure is that wind creates highly repetitive dynamic loading, which causes bending of the NSC-supporting beams that creates additional stresses on the anchors and consequently damage the NSC anchorage. If not considered, this damage can promote premature failure of the anchors below the design requirements. However, current code provisions used for anchor design (e.g. ACI318-14) are largely based on quasi-static single-anchor tests, which neglect the dynamic effects of strong wind loading, leading to potentially unsafe anchorage.

Aggravating this scenario, NSC anchorage is exposed to adverse environmental conditions common at the rooftop level during its service life. An important condition is elevated temperatures, which can exceed 75 °C on the rooftops in the U.S. (Winandy, 2002) and weaken the anchorage prior to the incidence of hurricanes. However, the elevated temperature effect has only recently been studied (e.g., Lahouar et al. 2017) and is not explicitly considered in design codes (e.g. ACI318-14). Another condition is the common presence of concrete cracking the rooftop level where most NSC are anchored. These cracks usually form over time due to the building's service loads and are attracted to the anchors during their installation, which damages their bond with the surrounding concrete. This condition is especially degrading for commonly-used adhesive anchors, in which the bond damage reduces their load capacity up to 50% (Eligehausen and Balogh, 1995). However, this effect is not captured by current anchor analysis, leading to overestimation of the load capacity of adhesive anchors damaged by concrete cracking.

To mitigate hurricane damage to NSC, it is initially necessary to understand and quantify the damaging influence of the bending of the NSC-supporting beams and the adverse environmental conditions on the NSC anchorage. Then, it is necessary to develop new recommendations to consider this damage during the anchor design and analysis.

1.1 Scope and Objectives

To advance the current anchor knowledge and mitigate hurricane damage to NSC, the following objectives are defined:

- To develop 3D high-fidelity nonlinear finite element models and verify them in the main anchor failure modes under static and dynamic tension and shear loads (typical during hurricanes). To employ the models to quantify the adverse effects of elevated temperature and concrete cracking on the anchor response and the influence of key design parameters on the load capacity of the anchors.
- To quantify the damage caused on the anchors due to the bending of the NSC-supporting beams by performing static and dynamic holistic analyses of an anchored NSC under strong wind. To develop new design recommendations in order to mitigate this damage.
- To develop and verify a 2D modeling approach, named "equivalent cone" approach, to enable the FE analysis of anchors using fast and simple 2D FE models while preserving the accuracy of the advanced 3D numerical models.
- To create, train, and test an artificial neural network with experimental data from a worldwide database to rapidly predict the load capacity of adhesive anchors damaged by concrete cracking with accuracy comparable to the FE analyses. To investigate the influence of the key input parameters on the ANN's load capacity predictions.

1.2 Outline of the Document

This document is organized as follows. Chapter 2 presents a review of the literature to introduce what research has been conducted and establish the current knowledge on the topic. Chapter 3 presents the 3D high-fidelity nonlinear finite element anchor modeling and its verification in the main anchor failure modes under static and dynamic tension and shear loading. The models are used to 1) quantify the adverse effect of elevated temperature and concrete cracking on the anchor response, and to 2) investigate the influence of key design parameters on the anchor performance. Chapter 4 presents holistic analyses of an NSC and its anchorage under static-equivalent and dynamic strong wind loading. The analyses allow the quantification of the damage caused on the anchors by the bending of the NSC-supporting beams. Design recommendations are presented to prevent this damage from causing premature failure of the anchorage. Chapter 5 presents a novel 2D modeling approach, named "equivalent cone" approach, developed to simplify and speed up the FE modeling of anchors by allowing accurate predictions of the anchor load capacity using 2D FE models only. The results obtained using this approach are compared to the 3D FE results presented in Chapter 3 and with existing experimental results to show that it provides similar accuracy to the 3D models. The equivalent cone approach is programmed into a spreadsheet, available to be easily used by researchers and engineers. Chapter 6 presents an artificial neural network (ANN) created, trained, and tested with an experimental worldwide database to predict the load capacity of adhesive anchors damaged by concrete cracking. The sensitivity of the ANN predictions to key input parameters is also investigated. The trained ANN is programmed into an open-access spreadsheet to be easily used by researchers and engineers. Chapter 7 presents the main conclusions of this study.

Chapter 2

Literature Review

Steel anchors have been extensively used in civil engineering to fasten NSCs and structures to concrete slabs. They typically consist of threaded rods that are bolted to the fastened component and installed into the concrete. Depending on the moment of installation with respect to the concrete hardening, anchors can be classified into two types:

- Cast-in place: Installed in fresh concrete.
- Post-installed: Installed after hardening of the concrete.

Anchors can be subdivided into four main categories: cast-in place headed anchors and post-installed undercut, expansion, and adhesive anchors (Figure 2-1). This study investigated headed and adhesive anchors since they comprise the most typical modes of failure, thus providing the most applicability to the findings.

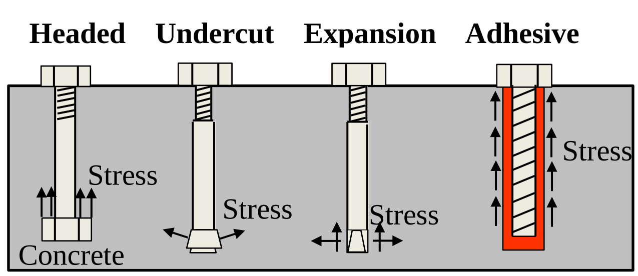

Figure 2-1: Main types of anchors and their load transfer mechanisms.

Headed anchors consist of cast-in place anchors containing a bolt on its embedded end that is responsible for most of its load resistance. Their installation consists of placement in fresh concrete, which hardens around it. When it is subjected to pullout (i.e. tension on the top), the load is mainly resisted by bearing stresses on the anchor's tip (Figure 2-1).

Adhesive anchors are a post-installed anchor installed with a chemical resin (also called chemical or adhesive) that acts as a glue, bonding the anchor to the concrete. Their installation consists of borehole drilling followed by cleaning, placement of the rod, and injection of the resin. They rely on the anchor-adhesive and adhesive-concrete bonds along their embedded length to resist the external load (Figure 2-1).

The main anchor failure modes under tension and shear loads considered in this study are shown in Figure 2-2. They consist of steel rupture in tension, concrete breakout, bond failure, and steel rupture in shear.

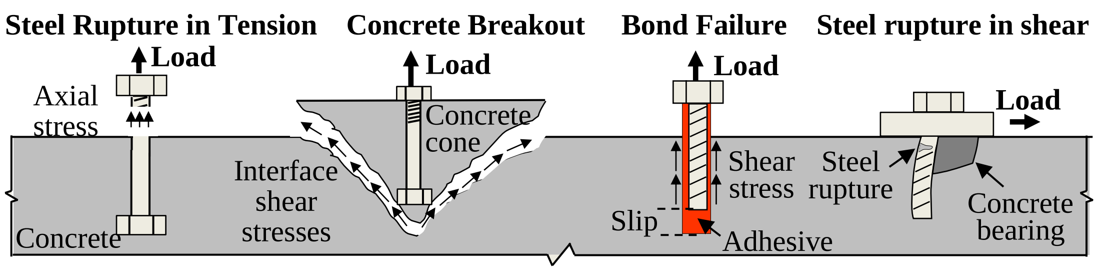

Figure 2-2: Main failure modes of anchors.

Steel rupture in tension is common for all types of anchors. It consists of the steel rod reaching its yielding and eventually ultimate stress, at which point the anchor breaks. Usually, the concrete has little to no participation. This mode is more common in headed anchors and more likely to happen in anchors with small diameter and large embedment depth, in which case there is a small area of steel and a large volume of concrete to resist the loads.

Concrete breakout is also common for all types of anchors. It is characterized by the pullout of a concrete trunk in a conical shape, frequently referred to as “concrete cone”. This mode is typical of shallow anchors with large diameters since these tend to experience large forces and the low embedment depth leaves little area of concrete to resist them. Furthermore, it is affected by the condition of the concrete before the load application (i.e. cracked vs uncracked), which can be captured by current numerical analysis techniques.

Bond failure is specific of adhesive anchors. It consists of pullout of the anchor due to the shear stresses along the steel-adhesive or adhesive-concrete interfaces exceeding the bond strength. The bond between the adhesive and the concrete is highly sensitive to the concrete condition (i.e. cracked vs uncracked), however, its effect is not captured by current numerical analysis techniques. In addition, the adhesive properties are affected by elevated temperature (Lahouar et al., 2017, 2018a, b, c).

Steel rupture in shear is common to all anchors and is characterized by bearing of the concrete, possibly followed by rupture of the steel in shear. For specimens located close to the concrete edges, spalling of the concrete can also occur. In this study, only specimens placed far enough from the concrete edges to prevent concrete spalling were considered.

2.1 The Present and Future Impact of Hurricanes

Hurricanes hitting the Atlantic U.S. coast have typically caused damage and detachment of anchored rooftop non-structural components and structures. The mitigation assessment team of the federal emergency management agency (FEMA) has reported substantial damage to HVAC units, electrical devices, and communication equipment placed on the roof of buildings during hurricane Katrina (FEMA, 2005). In the next year, another report by FEMA mentions the frequent detachment of rooftop equipment (FEMA, 2006). More recently, the agency has stated in an advisory that new observations after hurricanes Irma and Maria pointed to frequent damages to rooftop equipment once more and that the most common problems are related to improper anchorage (FEMA, 2018). Some of this damage is shown in Figure 2-3.

a) HVAC units blown off the roof after hurricane Irma

b) HVAC units blown off their curbs after hurricane Maria (holes were covered by plywood)

Figure 2-3: NSC detachment after hurricanes (a) Irma and (b) Maria (FEMA, 2018).

Solar panels are another common NSC susceptible to extreme wind. These are also commonly attached to the roof by steel anchors and can be detached if the anchorage is not done properly (Figure 2-4).

Figure 2-4: Solar panels blown away by a strong wind (Thurston, 2015).

Quantification of how much of the total hurricane damage is due to rooftop NSCs damage is complex. In addition to the direct cost of the affected equipment, there are monetary and environmental impacts associated with:

- Disposal of the debris.
- Repairing or manufacturing of new equipment.
- Delay in the restoration of critical services (e.g. hospitals).
- Building damage caused by water intrusion and wind coming through the roof.

Cope (2004) estimated that 35% of the total post-hurricane cost in Central Florida was due to the repair of NSCs only. Similar values have been reported for earthquakes, when damage to NSCs in a facility can account for 50% of its value, excluding clean-up costs and recovery delay (Griffin and Winn, 2009). The authors also stated that inadequate anchorage is the main issue causing poor NSC seismic performance.

The total damage caused by hurricanes tends to increase in a scenario of progressive coastal development and climate change, with estimates that the current yearly average post-storm cost of $28 billion can reach $151 billion by 2075 (with reference monetary values of 2015) (Dinan, 2017). Although there is some uncertainty regarding the future frequency of hurricane events, many researchers agree that hurricanes tend to become more destructive and major hurricanes (i.e. categories 3 and above in the Saffir-Simpson scale) will likely strike more often (e.g., Dinan, 2017; Knutson, 2013; Emanuel, 2013). Webster et al. (2005) have studied the quantity, duration, and intensity of tropical cyclones over 35 years and found an increase in the number of hurricanes categories 4 and 5 with an increasing trend in frequency and duration in the Atlantic at a confidence level of 99%. Emanuel (2005) looked into the evolution of the destructive power of hurricanes, concluding that even though their frequency did not present an increasing trend, longer-lasting and larger storms related to higher sea surface temperatures (SST) have been causing the total storm destructiveness to grow since the mid-1970s. Kossing et al. (2007) constructed a hurricane intensity database that supports the findings of Webster and Emanuel regarding the hurricane trends in the Atlantic.

Since tropical storms need warm ocean water to form, researchers have investigated a potential correlation between higher SST and more frequent or stronger storms. Villarini and Vecchi (2012) studied the trends in ocean temperature and tropical storms in the 21st century and concluded that a projected increase in storm frequency in the Atlantic was related to a higher temperature of this ocean with respect to the tropics. Cui and Caracoglia (2016) examined several projections of global surface temperature change for the next hundreds of years and reasoned that with the tendency of higher temperatures more intense hurricanes are expected to reach the coast of the U.S, a conclusion supported by previous studies (e.g. Mudd et al., 2014). The authors performed numerical simulations on hurricanes (validated with historical data) in different climate change scenarios and found that although several factors influence hurricane frequency, the use of SST as the only factor is acceptable due to its high importance. They used a linear regression model based on SST to predict future hurricane intensity.

To reduce the potential impact of storms on NSCs, past research has been conducted to determine the wind loads acting on anchored appurtenances. Hosoya et al. (2001) performed wind tunnel experiments on an HVAC of reduced scale 1:50, which resulted in changes in the ASCE7 code from the 2002 to the 2005 version. Afterward, Erwin et al. (2011) carried on similar but full-scale experiments using the Wall of Wind facility at Florida International University. They found uplift and lateral forces larger than expected, which was attributed to the increased height of their equipment, and significant overturning moments. Thus, they suggested additional studies to assess the adequacy of design codes.

2.2 Past Research on Anchorage

Many studies have been conducted on anchorage behavior in the last decades covering all types of anchors in several loading, environment, and installation conditions. Most investigations consisted of experimental or numerical analysis of anchors under static tensile loading, however, a few included dynamic loading as well. Some studies considered shear, while the majority only explored tensile loading. Some researchers analyzed the influence of installation conditions (e.g. uncracked vs cracked concrete, near/far to the slab edge) and a limited number of recent studies investigated the effects of low and high temperature on adhesive anchors. Several of these studies are summarized below.

2.2.1 Studies on Anchors under Static Pullout Loading

Most research investigated the pullout behavior of single anchors under monotonic static loading, while some studies considered anchors groups and sustained loads. Experiments and FE analysis are among the most popular approaches.

McVay et al. (1996) performed finite element (FE) pullout simulations of adhesive anchors with varying embedment depths and conducted experiments to validate the FE models. They observed concrete breakout in anchors with low embedment depth, while bond failure prevailed for deeper ones. Furthermore, they found the uniform bond stress model to be the best predictor of bond capacity among the models studied and pointed out that the bond stress becomes more uniform with increased embedment depth.

Cook et al. (1998) confirmed the appropriateness of a uniform bond model as they developed a general anchor design approach. They compared existing design methods with a worldwide database and found a model that fits well the data for adhesive anchors installed in clean and dry boreholes and far from the edges of an uncracked concrete slab. The scientists noted that all available tests had been conducted at room temperature and reduction of the adhesive strength could be necessary for higher temperatures.

Eligehausen et al. (2006) proposed a behavioral model for adhesive anchors installed in uncracked concrete in groups and/or near edges. They derived equations to calculate the anchor capacity and a critical spacing beyond which group effects are not observed. The model developed showed good agreement with numerical and experimental results from a worldwide database involving 415 tests on adhesive anchor groups and 133 tests of adhesive anchors near edges.

Tsavdaridis et al. (2016) performed numerical analyses of headed anchors as part of a study regarding base plate connections subjected to biaxial moment with a large number of anchor rods. The models were validated with experimental data and used in a parametric study varying the anchor diameter, embedment depth, and anchor head size. They observed steel rupture in specimens with large embedment depths while concrete breakout was present in shallower specimens, with the concrete cracking developing in an angle of approximately 35° with the horizontal.

Nilforoush et al. (2016) tested adhesive anchors under sustained tensile loading indoors and outdoors. Experiments performed at load levels of 23%, 47%, and 70% of the short-term capacity revealed that the indoor anchors did not fail under sustained loads up to the 47% level, while the outdoor anchors failed above the 23% level. They related the reduced load capacity and an increased level of creep observed in outdoor anchors to temperature and humidity variations. Furthermore, multiple adhesive systems were tested and found to have significantly different creep behaviors. The authors recommended that load versus time-to-failure tests be incorporated in approval standards for improved safety in sustained load applications.

Nilforoush et al. (2017) numerically examined the tensile capacity of headed anchors in uncracked concrete of multiple embedment depths and for three head sizes. The results were compared with predictions from various code equations. Design methods were found to underestimate the concrete breakout ultimate load for anchors with large heads and modification factors were suggested. In addition, higher load capacities were obtained for larger heads, however with lower ductility. Lastly, larger anchor heads promoted concrete cone diameters of $5h_{ef}$, considerably above typical values. It was advised that the recommended spacing for groups of anchors with this characteristic be increased.

Çaliskan and Aras (2017) performed static pullout tests on adhesive anchors with various diameters, embedment depths, and bonding chemical types. A total of 10 chemicals were used, including four epoxy, three polyester, two epoxy acrylics, and one vinylester. The prevalent failure modes were steel rupture and concrete breakout. The authors found that the chemical type affected anchors with embedment depth greater than 10 times the bar diameter, the effect being more pronounceable in anchor with large diameters (> 20 mm). They pointed out that ACI318 does not consider the type of adhesive in design equations, despite its importance.

Marcon et al. (2017) developed a lattice discrete particle model (LDPM) and validated it with experiments on adhesive anchors in confined and unconfined conditions. The model was proposed as an alternative to traditional simulation techniques with the advantages of providing more realistic and unbiased cracking patterns, localization of damage in zones of high strains and stresses, and a predictive model for adhesive to account for change in properties over time, at the cost of higher computational requirements due to the impossibility of taking advantage of symmetry. The LDPM was able to accurately predict the load capacity, crack pattern, and failure mechanism observed experimentally.

Wang et al. (2017) performed experiments and used numerical analysis to assess the pullout response of adhesive anchors with large bar diameters (36-150 mm) and embedment depths of $8d_a$ and $12d_a$. The authors divided the obtained load-displacement curves into four regions: elastic deformation, nonlinear deformation, concrete crack, and anchor failure. They also found that the load capacity was more sensitive to the thickness of the adhesive than to the anchor diameter for adhesive thickness above 25 mm.

2.2.2 Studies on Anchors under Dynamic Pullout Loading

Although rarer, some studies have experimentally investigated the behavior of single anchors under dynamic pullout loading.

Sato et al. (2004) investigated the effect of the loading rate in the capacity of headed and adhesive anchors in uncracked concrete. They performed rapid monotonic pullout tests at four loading rates varying from 0.1 kN/s to 40,000 kN/s in an unconfined setup for headed anchors and confined for adhesive in order to capture the failure modes of concrete breakout and bond failure. The authors found that in both cases the capacities increased with the loading rate, with the effect being more pronounced for concrete breakout, and proposed equations to calculate the dynamic-to-static capacity ratio.

Solomos and Berra (2006) tested headed studs, undercut, and adhesive anchors under monotonic dynamic pullout loading simulating impact and blast conditions. The obtained results were compared with code predictions by ACI318-02 and the concrete capacity design (CCD) approach. The dynamic load capacities were found to be up to 67% higher than their static counterparts, which was higher than predicted by code provisions at the time. The authors attributed this effect to a possible increase in the ratio of tensile to compressive concrete strength in the dynamic regime. They also highlighted that post-installed anchors were able to achieve load capacities as high as cast-in-place ones.

2.2.3 Studies on Anchors under Static Shear Loading

Experimental and finite element techniques have also been applied to investigate the single-anchor and group anchor response to static shear loading. Anchors near and far from the concrete edge were considered. In the former case, the effect of supplementary reinforcement was studied.

Kim et al. (2013) evaluated the tensile and shear load capacity of post-installed anchors. For that purpose, the authors performed experimental tests in anchors with varying diameters, embedment depths, and applied installation torque and 3D FE analysis. The researchers found that increasing the torque did not enhance but sometimes decreased the tensile or shear strength of the specimens.

Caliskan et al. (2013) studied the shear capacity of adhesive anchors installed into low-strength concrete. The authors tested anchors with varying bar diameter and embedment depth in 5 MPa and 10 MPa uncracked concrete under reversed cyclic shear loading. They found that anchors with larger diameters have higher load capacity, however, fail at lower shear stress levels. They also compared the results with ACI318-05 predictions and concluded that ACI equations provided safe predictions, but the factor of safety decreased with increasing anchor diameter. In response to that, they proposed a correction factor for large diameters.

Epackachi et al. (2015) performed static pullout and shear tests on adhesive anchors and compared the load capacity with predictions by ACI318-14 and other equations from the literature. Single anchors and groups of anchors were considered with varying spacing and number of anchors in the group. The authors concluded that the selected equations predicted the load capacity better than ACI, which underestimated them.

Sharma et al. (2017) conducted experiments to find the shear capacity of anchor groups close to a concrete edge with and without supplementary reinforcement. They found that the presence of supplementary reinforcement greatly increased the anchorage capacity and that predictions by multiple codes were overly conservative for low amounts of reinforcement and unsafe for high amounts. They announced the development of a rational model to account for that in a future paper.

2.2.4 Studies on Anchors exposed to Concrete Cracking

It is reasonable to imagine that concrete cracking can affect the strength of the anchors connected to it. To investigate that, researchers have tested anchors installed in concrete with different crack widths under static and dynamic pullout loading. Crack cycles have also been applied to simulate seismic activity.

Hoehler et al. (2011) tested expansion and adhesive anchors in cracked concrete under monotonic quasi-static and dynamic tensile loading. Cracks of 0.5 mm and 0.8 mm width were created in a concrete slab at the points where the anchors were installed, and tensile loading was applied at rising times that varied from 1-3 min for quasi-static until 0.02 sec for dynamic. The authors concluded that higher loading rates increased the load capacity of concrete breakout and bond failures, the former growing faster. Therefore, tests above the quasi-static rate would not be necessary for design purposes, although a change in failure mode can occur as the rate changes.

Mahrenholtz et al. (2014) investigated the behavior of post-installed anchors supporting suspended NSCs attached to the bottom of a cracked concrete slab under earthquake loading. They performed experiments using a shake table and found that anchor displacement may accumulate during the shaking up to several millimeters. The authors also pointed out that, according to previous studies, damage to NSCs can be started at deformation levels much smaller those required to initiate structural damage.

Mahrenholtz et al. (2017) studied the response of post-installed anchors under sustained tensile load using a stepwise crack cycle protocol to simulate the opening and closing of concrete cracking during seismic activity. They found adhesive anchors to be among the most damaged types during the crack cycles, which was attributed to damage to the micro-interlock of these anchors.

2.2.5 Studies on Adhesive Anchors exposed to High Temperature

While most anchor types are not significantly affected by fluctuations in temperature, adhesive anchors can be highly sensitive to them due to softening of their resin with consequent degradation of the anchor’s strength and stiffness at elevated temperatures. These resins are typically thermosetting, being in a liquid state at room temperature but hardening upon curing. Although adhesive anchors are used for applications involving a range of temperatures, the effect of elevated temperatures on their behavior has only recently been studied.

Fuchs et al. (2016) investigated the effect of several curing conditions, especially low-temperature curing, on the tensile strength of adhesive anchors. Several anchors were tested under sustained and short-term static pullout loads. Epoxy and vinylester were used as the resin. The adhesive temperature was increased after its initial curing, causing what the authors called post-curing. This post-curing was observed to increase the tensile load capacity of the anchors and reduce creep rates.

Lahouar et al. (2017) studied the effect of elevated temperatures on the mechanical properties of adhesives and on the response and load capacity of adhesive anchors. They found an increase in bond strength with increasing temperatures up to a point due to post-curing of the adhesive. However, beyond ~50 °C the elevation in temperature reduced the bond strength. Moreover, the increase in temperature was shown to decrease the anchor load capacity and stiffness of the adhesive anchors tested.

Lahouar et al. (2018a) studied the mechanical behavior of glued-in steel rods bonded to wood under pullout loading at constant temperature (increasing load) and constant load (increasing temperature). The anchors were bonded parallel and perpendicular to the wood grains. They found a significant decrease in bond strength at service temperatures, with a 65% reduction at 50 °C when compared to the strength at 20 °C.

Lahouar et al. (2018b) developed a nonlinear shear-lag model to predict the stress distribution in chemical anchors accounting for the effect of the temperature profile along the anchor embedded depth. The model was validated with experimental measurements and permits the prediction of damage initiation and the affected adhesive length.

Lahouar et al. (2018c) conducted tests on slab attached to a wall through post-installed bonded rebars and subjected to ISO 834-1 fire conditions. Degradation of the bond properties with the temperature increase caused the slab to collapse after 117 min of heating, a time that was accurately predicted by design provisions.

2.2.6 Artificial Intelligence Applications to Anchors

Despite the widespread use of finite element analysis to simulate anchor behavior, studies using artificial intelligence (AI) have also been conducted to predict the load capacity of anchors. This approach has the advantage of being easy-to-use, and able to calculate the anchor capacity quickly. On the other hand, the result obtained is limited by the defined output, typically the load capacity and/or anchor displacement, and to the range of parameters used to train (i.e. calibrate) the AI.

Ashour and Alquedra (2005) developed an artificial neural network to predict the concrete breakout capacity of cast-in and post-installed single anchors under tension. The ANN was trained with experimental data from worldwide databases. The authors concluded that ANNs are a viable resource to predict the concrete breakout capacity.

Sakla and Ashour (2005) created an artificial neural network to determine the bond stress in adhesive anchors under tension using a uniform bond assumption. The network was trained with specimens installed in uncracked concrete only, therefore it is not applicable to specimens damaged by concrete cracking. They found the uniform bond model to yield accurate load predictions and compared the strength of different types of resin.

Gesoglu and Guneyisi (2007) used neural network and genetic programming (GP) techniques to generate a closed-form solution to predict the load capacity of adhesive anchors in uncracked concrete under tension. The ANN provided the best correlation to experimental results while the GP generated the most user-friendly solution. Both methods had more accurate predictions than those given by the CCD method and generate a final equation that could be used for single-anchor design or capacity assessment.

Gesoglu et al. (2014) used gene expression programming (GEP) to predict the edge breakout capacity of adhesive anchors in uncracked concrete under shear. The developed algorithms provided more accurate predictions than ACI318-08 provisions.

Guneyisi et al. (2016) developed a neural network to capture the edge breakout capacity of adhesive anchors in uncracked concrete under shear. According to the authors, the ANN developed was simpler than most available models and provided accurate load predictions.

2.3 State-of-the-Art and Research Gaps

Despite the extensive research on anchorage, some points remain to be addressed based on the studies found. For one, most studies on adhesive anchors have been conducted in uncracked concrete at room temperature, despite the presence of elevated temperatures and concrete cracking in typical anchor applications, which have a significant impact on the load capacity of adhesive anchors (Lahouar et al., 2017; Eligehausen and Balogh, 1995). There is also a need for an analysis method that captures the concrete cracking effect on the bond strength of adhesive anchors, which is neglected by the typically used FE analysis.

In addition, anchors are typically analyzed independently of the anchored NSC. This approach ignores the damage caused by the bending of the NSC-supporting beams during strong wind and wind-induced simultaneous tension and shear action, which significantly affect the performance of the anchorage during hurricanes.

Lastly, it was observed that FE analysis of anchors is typically done using 3D FE models to capture the concrete breakout load capacity due to the three-dimensional stress and strain distributions in this mode. Alternatively, the use of 2D FE models is desired since they are simpler, have shorter analysis time, and are less computationally expensive.

The present study attempted to address these points.

2.4 State-of-the-Practice

The design of anchors supporting NSC subjected to strong winds is currently performed by calculating the wind loads on the NSC anchorage according to ASCE7-16 provisions and designing each anchor to resist the loads according to ACI318-14. Alternatively, technical guides such as the Hilti catalog (Hilti, 2017) can be used to choose the anchor size (and adhesive type, for adhesive anchors) based on the desired load capacity. These design practices are largely based on experimental results from quasi-static single-anchor tests, which neglect the damage caused on the anchors by the bending of the NSC-supporting beams during hurricanes. Furthermore, the adverse effects of elevated temperature and concrete cracking are considered by permitting the use of a minimum bond strength regardless of the severity of these conditions, which may be over-conservative.

On the other hand, the analysis of anchors is commonly done using more advanced techniques, such as finite element analysis. However, it is not clear how to consider the adverse effect of elevated temperature in this type of analysis and the adverse effect of concrete cracking on the bond of adhesive anchors is not captured by the finite element.

This study has the potential to impact the current practice of anchor design and analysis in several ways. For one, 3D high-fidelity nonlinear FE models of single anchors are developed, verified in the main anchor failure models, and used to show how to account for the adverse temperature effect using FE anchor models. Secondly, holistic analyses of an anchored NSC subjected to strong wind are used to quantify the damage caused by bending of the NSC-supporting beams on the anchors and new design recommendations are developed based on the results to mitigate this type of damage, preventing premature anchor failure. In addition, a novel 2D modeling approach named "equivalent cone" approach is developed to permit the numerical analysis of anchors to be performed using simpler and faster 2D FE models only. The approach is verified with the results of the 3D FE models and existing experiments to show that it preserves the accuracy of the 3D FE models while being less computationally demanding. Lastly, an artificial neural network is developed to quickly and accurately assess the load capacity of adhesive anchors damaged by concrete cracking. The ANN is trained and tested with over one hundred experimental results from the worldwide database kept by ACI Committee 355 to provide the most generality to its predictions. The trained ANN is able to predict the anchor capacity with an accuracy comparable to its FE counterpart in a short time (i.e. usually less than a second) and is programmed on an open-access spreadsheet that can be easily used for design or combined with numerical techniques to improve the anchor analysis.

Chapter 3

Creation and Verification of Single-Anchor Finite Element Models

To establish a finite element approach for anchor modeling, high-fidelity nonlinear FE models are created and verified in the main anchor failure modes under pullout and shear loading (i.e. steel rupture in tension, concrete breakout, bond failure, and concrete bearing followed by steel rupture in shear) with experimental data from the literature.

3.1 Compilation of Experimental Data

A total of 14 anchor specimens tested in pullout and shear were selected from the literature and analyzed using the FE software Abaqus. Tables 3.1 to 3.4 present all the selected specimens, their paper of origin, and geometric and material properties.

Table 3.1: Geometric information of the modeled specimens and their paper of origin.

Paper of origin	Specimen	Type	d_a (mm)	h_{ef} (mm)	d_{hole} (mm)	d_{tip} (mm)	h_{tip} (mm)
Tsavdaridis (2016)	D20L200W70	Headed	17.0	200	17.0*	70	20*
	D20L400W70	Headed	17.0	400	17.0*	70	20*
	D20L800W70	Headed	17.0	800	17.0*	70	20*
	D16L160W56	Headed	14.4	160	14.4*	56	20*
	D16L320W56	Headed	14.4	320	14.4*	56	20*
	D20L100W70	Headed	17.0	100	17.0*	70	20*
	D16L80W56	Headed	14.4	80	14.4*	56	20*
Eligehausen (1992)	D24H150	Headed	24.0	150	24.0*	33	20*
	D72H450	Headed	72.0	450	72.0*	88	20*
Nilforous (2017)	NPC440	Headed	36.0	220	36.0*	55	30
Hoehler (2011)	Ae12	Adhesive	12.0	60	14.0*	N/A	N/A

Paper of origin	Specimen	Type	d_a (mm)	h_{ef} (mm)	d_{hole} (mm)	d_{tip} (mm)	h_{tip} (mm)
Epackachi (2015)	D20H200	Adhesive	20.0	200	24.0	N/A	N/A
Marcon (2017)	D12H70	Adhesive	12.0	70	14.0	N/A	N/A

*Estimated values due to lack of data provided.

Table 3.2: Material properties of the modeled specimens – concrete.

Specimen	Condition	E_c (MPa)	f'_c (MPa)	f'_t (MPa)	w_{cr} (mm)
D20L200W70	Uncracked	23500*	25.00	1.65*	0.00
D20L400W70	Uncracked	23500*	25.00	1.65*	0.00
D20L800W70	Uncracked	23500*	25.00	1.65*	0.00
D16L160W56	Uncracked	23500*	25.00	1.65*	0.00
D16L320W56	Uncracked	23500*	25.00	1.65*	0.00
D20L100W70	Uncracked	23500*	25.00	1.65*	0.00
D16L80W56	Uncracked	23500*	25.00	1.65*	0.00
D24H150	Uncracked	26200	27.71	2.97	0.00
D72H450	Uncracked	26200	27.71	2.97	0.00
NPC440	Uncracked	27440*	34.09	3.2	0.00
Ae12	Cracked	21965*	21.84	1.54*	0.50
D20H200	Uncracked	32508*	47.84	2.28*	0.00
D12H70	Uncracked	22310	25.96	2.71	0.00

*Estimated values due to lack of data provided.

Table 3.3: Material properties of the modeled specimens – steel.

Specimen	E_s (MPa)	f_y (MPa)	f_u (MPa)	ε_{sh} (me)	ε_u (me)
D20L200W70	218000	434	524	0*	22.5*
D20L400W70	218000	434	524	0*	22.5*
D20L800W70	218000	434	524	0*	22.5*
D16L160W56	218000	434	524	0*	22.5*
D16L320W56	218000	434	524	0*	22.5*
D20L100W70	218000	434	524	0*	22.5*
D16L80W56	218000	434	524	0*	22.5*
D24H150	200000*	500*	500*	10*	150*
D72H450	200000*	500*	500*	10*	150*
NPC440	200000*	900	1000	10*	150*
Ae12	200000*	500*	500*	10*	150*
D20H200	200000*	640	800	10*	150*
D12H70	200000*	1080	1200	10*	150*

*Estimated values due to lack of data provided.

Table 3.4: Material properties of the modeled specimens – adhesive.

Specimen	Type	τ_a (MPa)	E_a (MPa)
Ae12	Epoxy	N/A	50.00*
D20H200	HIT-HY 150	16.94	17.65*
D12H70	Mortar	22.55	30.89

*Estimated values due to lack of data provided.

From the specimen selection, it was noted that most tests are performed in uncracked concrete. Examples of typical 2D and 3D FE models are shown in Figure 3-1. The geometric parameters listed in Table 3.1 are illustrated in Figure 3-1a.

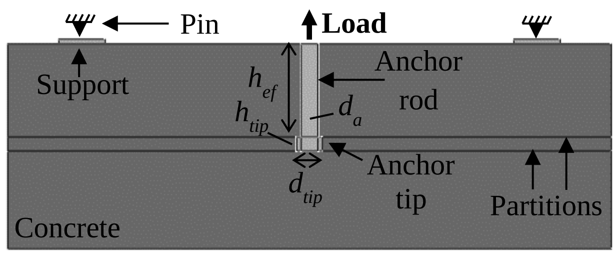

a) 2D model example

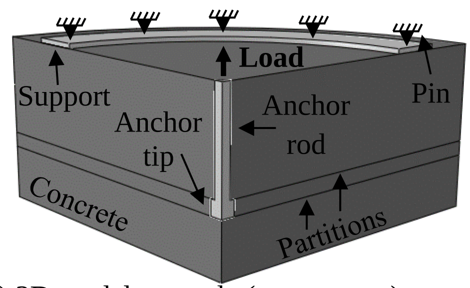

b) 3D model example (one-quarter)

Figure 3-1**:** Typical (a) 2D and (b) 3D anchor models and main geometric parameters.

When not given in the literature, the longitudinal modulus of elasticity and tensile strength of the concrete were calculated according to Eqs. 3.1 and 3.2 from ACI318-14.

$$E_c = 4700\sqrt{f'_c} \qquad (3.1)$$

$$f'_t = 0.33\sqrt{f'_c} \qquad (3.2)$$

3.2 Verification of the Finite Element Models for Static Loading

Two- and three-dimensional FE models are used to analyze the behavior of single anchors. Due to the low computational demand of 2D models, the entire specimen is modeled in them. Four-node 2D stress solid elements (CPS4R) are used to model the steel rod, support/loading plates, and the concrete. On the other hand, 3D models are more computationally and time demanding, therefore, to take advantage of symmetry and reduce the high analysis time taken by 3D models, only one-quarter of the specimens is modeled in them. In this case, appropriate boundary conditions are applied to the planes of symmetry (i.e. restraining axial forces and moments around the axis in the plane). Eight-node 3D stress solid elements (C3D8R) are used for the steel rod and the concrete. In adhesive anchors, cohesive elements (COH2D4 for 2D and COH3D8 for 3D) are used to model the adhesive, as recommended for “glue-like” materials (Abaqus, 2014).

The concrete damaged plasticity (CDP) approach is used to simulate the concrete behavior due to its ability to capture the concrete crushing in compression and cracking in tension (Wahalathantri et al., 2011). The Hognestad parabola is used to define the stress-strain relationship in compression, while the tension softening described in (Wahalathantri et al., 2011) is used to define the post-crack tensile behavior (Figure 3-2a, b). The steel response is simulated by a typical elastic-plastic formulation accounting for nonlinear strain hardening according to the Menegotto-Pinto model (Wong et al., 2002) (Figure 3-2c). The adhesive bond behavior is uniformly defined throughout the anchor length and follows a trilinear backbone with an elastic branch, peak strength plateau, and linear post-peak softening according to the Eligehausen model (Wong et al., 2002) (Figure 3-2d).

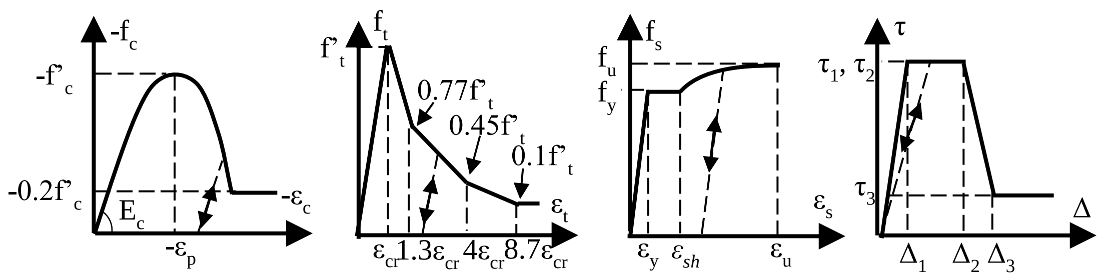

a) Concrete in compression b) Concrete in tension c) Steel behavior d) Adhesive behavior

Figure 3-2: Material models used in the numerical analyses.

The support conditions vary according to the experimental setup used but typically consist of either fixing the bottom and sides of the concrete block or placing pinned steel supports on top of the concrete, as shown in Figure 3-1. In adhesive anchors, the top of the concrete is also restrained to simulate confined test conditions. In the pullout analyses, uplift displacement is applied at the tip of each of the 13 specimens to capture their post-peak response. In the shear analysis, the anchor is extended above the top of the slab and connected to a steel plate for the load application, which consists of lateral displacement applied to the top of the plate. The steel plate is modeled as linear-elastic since it is not expected to significantly influence the model. The supports, in this case, consist of pins along the edges of the slab.

To avoid over predicting the anchor initial stiffness, friction between the anchor rod and the concrete is neglected. This is believed to be realistic due to the formation of small cracks around the anchor upon loading. A hard contact interaction between the anchor and the concrete is defined to avoid interpenetration between them.

Five of the specimens shown in Table 3.1 present rupture of the steel as the failure mode, named: D20L200W70, D20L400W70, D20L800W70, D16L160W56, and D16L320W56. The boundary conditions in these specimens consisted of fixed bottom of the concrete, as per their paper of origin and restrained edges with horizontal rollers to prevent splitting of the concrete.

In the steel rupture failure mode in tension, elongation of the anchor rod was observed as the steel yields and strain hardening occurs, with eventual rupture of the rod when the steel reaches its ultimate capacity (Figure 3-3). In the 2D models, the rupture occurred near the bottom of the anchor with little engagement of the concrete (Figure 3-3b).

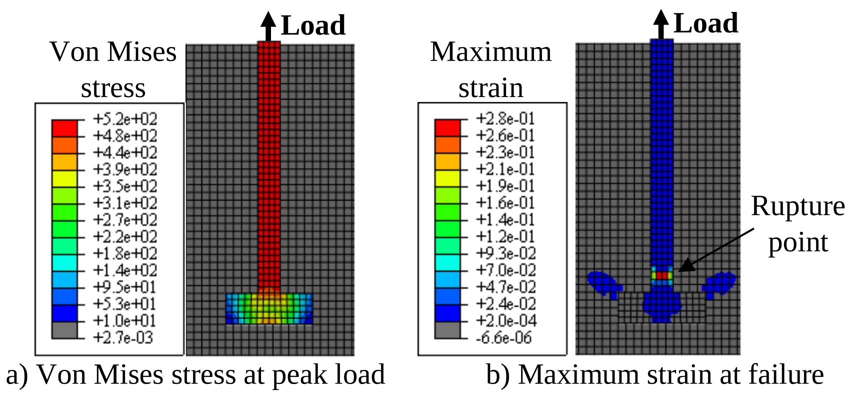

Figure 3-3: D16L160W56 2D deformed shape and stress at (a) peak load and (b) failure.

The response of the 3D models was similar to the 2D models, however, the steel rupture occurred at the top of the anchor (Figure 3-4), which is the behavior typically observed in experiments. The 3D models also presented little engagement of the concrete.

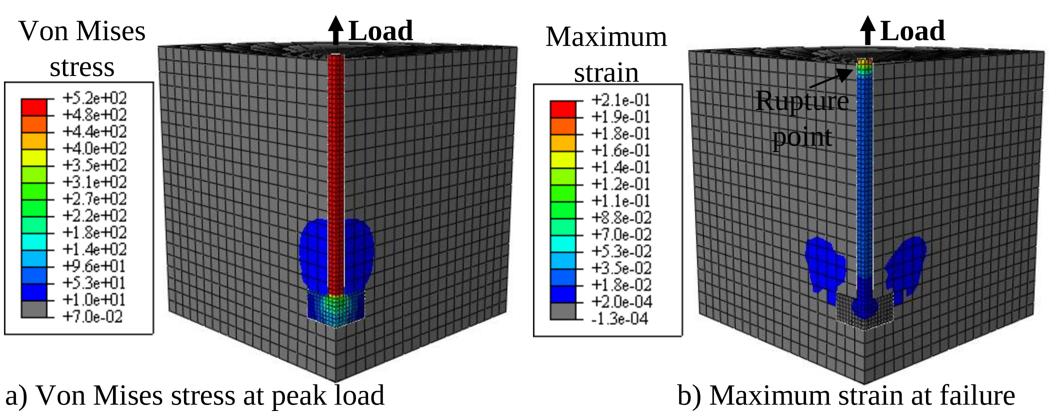

Figure 3-4: D16L160W56 3D deformed shape and stress at (a) peak load and (b) failure.

The 2D models provided a good peak load agreement with the experimental data, however, they underestimated the ductility of the anchors (Figure 3-5). The 3D FE predictions agreed with the experimental results, predicting the overall response correctly, including initial stiffness, yielding point, peak load, and displacement at failure (Figure 3-5). Based on these results, the modeling approach was considered verified for steel rupture.

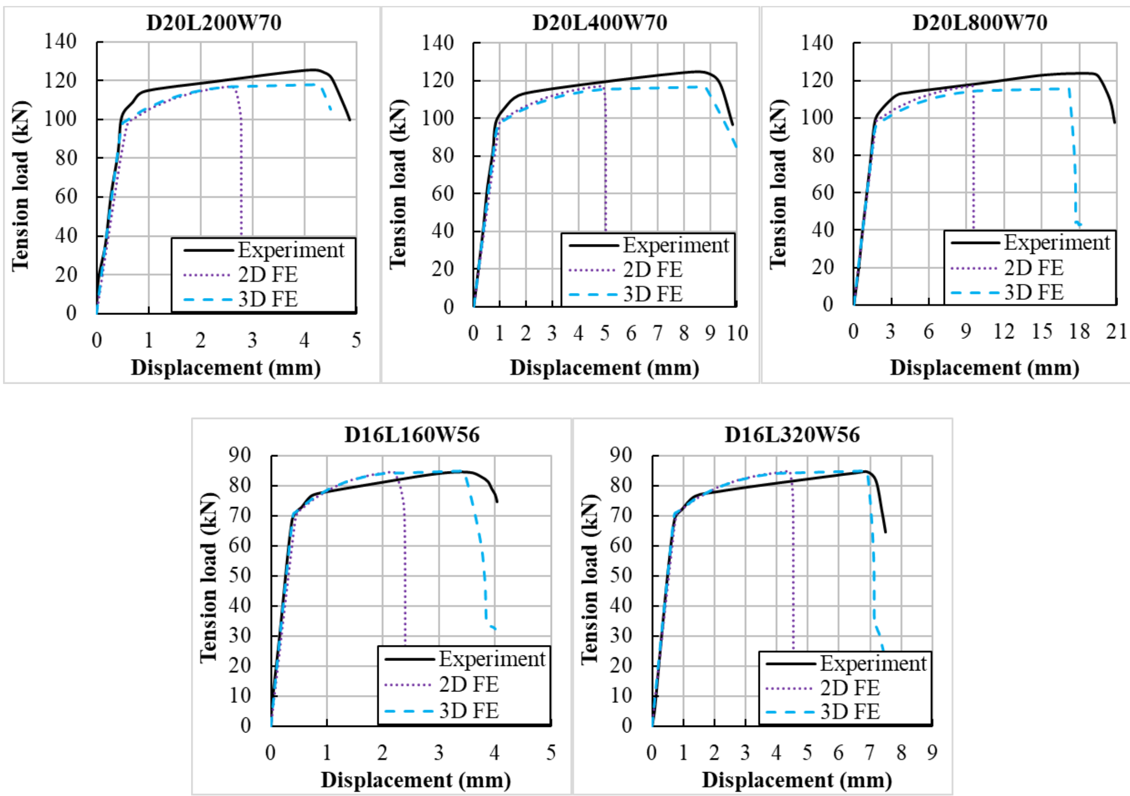

Figure 3-5: Load-displacement curves for steel rupture in tension.

Six of the specimens shown in Table 3.1 fail in concrete breakout, namely: D20L100W70, D16L80W56, D24H150, D72H450, NPC440, and Ae12. Their boundary conditions consisted of fixing the bottom and sides of the concrete block for specimens D20L100W70 and D16L80W56, while in the other cases pinned steel plates were placed on top of the concrete, according to each specific experimental setup. A minimum distance of $1.5h_{ef}$ was kept from the center of the anchor to the center of the support plates to allow the formation of a complete concrete cone, according to recommendations from ACI318-14, and as done in the literature.

When creating 2D FE models for concrete breakout, there is a challenge regarding the definition of the concrete thickness. 2D FE models typically consider all phenomena (e.g. cracking and stresses) to be constant over the thickness, however, this does not correspond to reality in concrete breakout, as the concrete breaks a conical shape. Therefore, the concrete thickness must be properly defined to accurately predict the concrete breakout capacity. In the creation of the 2D models for concrete breakout in this study, the concrete thickness is defined according to the developed equivalent cone approach, which is presented in Chapter 5 and verified with the results from 3D models shown here.

In the concrete breakout mechanism in tension, high concrete stresses form around the anchor and dissipate in a conical shape towards the supports. The failure occurs at a low displacement level (i.e. brittle) with cracking of the concrete occurring conically, starting at the anchor tip and progressing towards the top of the concrete (Figures 3-6 and 3-7), which is in good agreement with typical experimental observations. The load-displacement responses have a good match with those reported in the literature (Figure 3-8), verifying this mechanism. Noticeably, the initial stiffness was better captured by the 3D models, especially in specimens D20L100W70 and D16L80W56. In the other cases, the analysis slightly overestimated the stiffness of the response.

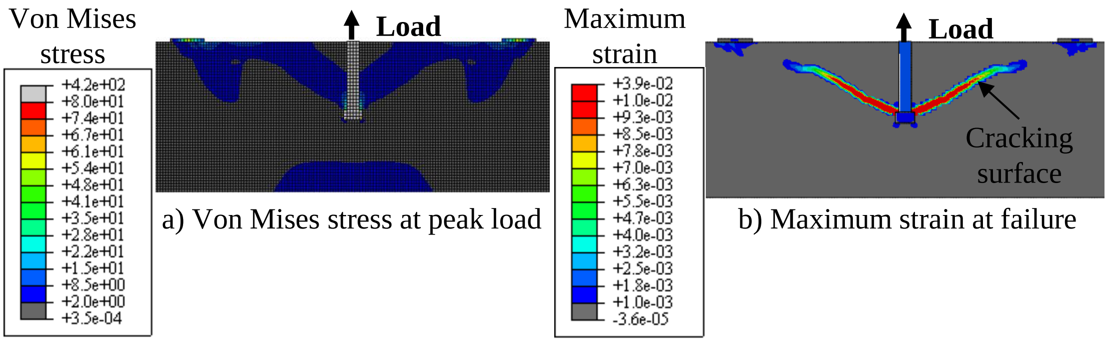

Figure 3-6: NPC440 2D deformed shape and stress at (a) peak load and (b) failure.

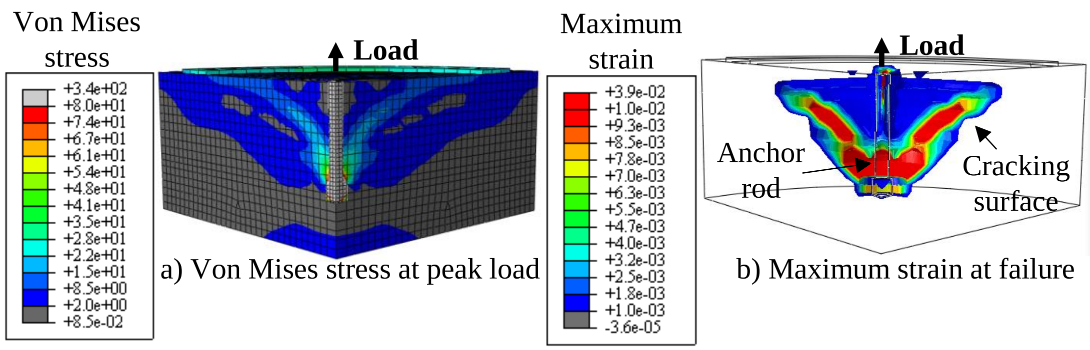

Figure 3-7: NPC440 3D deformed shape and stress at (a) peak load and (b) failure.

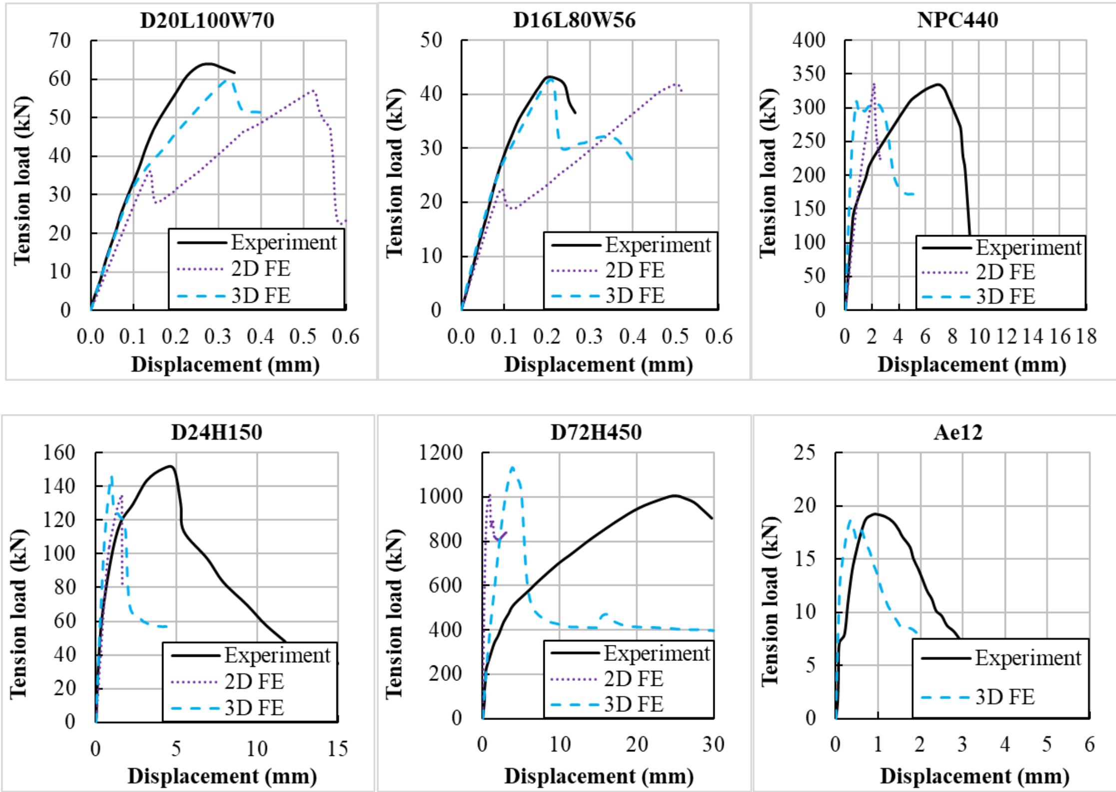

Figure 3-8: Load-displacement curves for concrete breakout.

The bond failure mode occurs in the two adhesive specimens from Table 3.1 and is characterized by slipping of the anchor upwards as the adhesive reached its strength (Figures 3-9 and 3-10). Little engagement of the concrete and no yielding of the steel are observed, meaning that the anchor response is dictated mostly by the bond stress-slip relationship. The numerical responses obtained presented a good agreement with the experimental load-displacement data for both 2D and 3D FE models, therefore verifying this mechanism (Figure 3-11).

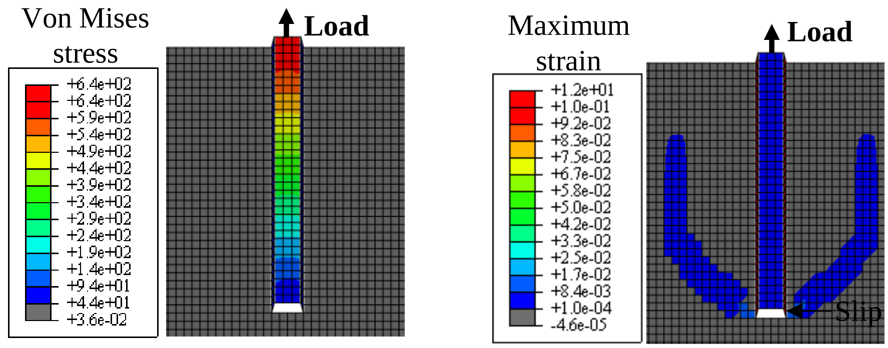

a) Von Mises stress at peak load b) Maximum strain at failure

Figure 3-9: D12H70 2D deformed shape and stress at (a) peak load and (b) failure.

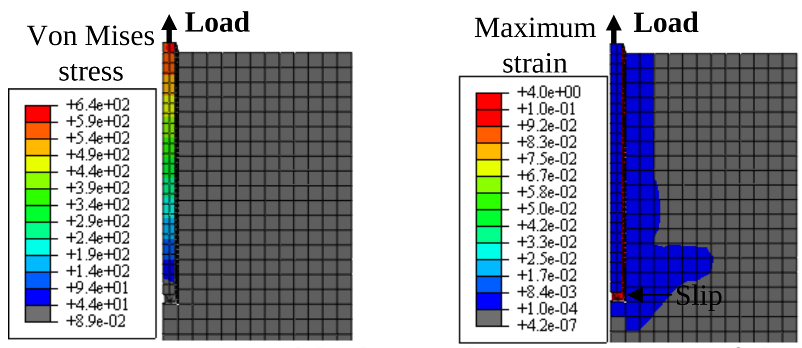

a) Von Mises stress at peak load b) Maximum strain at failure

Figure 3-10: D12H70 3D deformed shape and stress at (a) peak load and (b) failure.

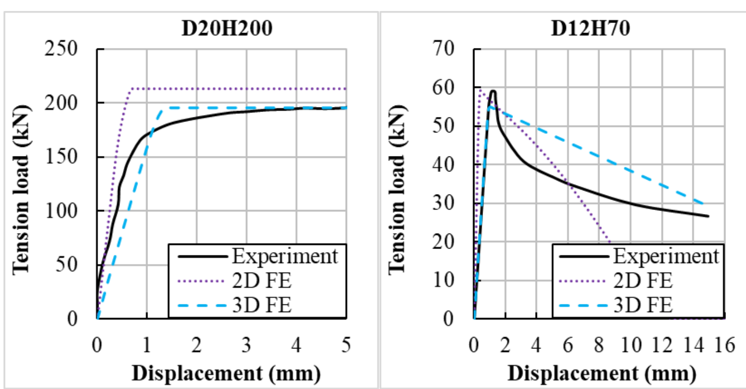

Figure 3-11: Load-displacement curves for bond failure.

Steel rupture in shear is present in model D20H200 when it is subjected to shear loading. The geometry of the 2D and 3D models are shown in Figure 3-12. In this case, the highest stress occurs in the anchor rod, resulting in steel rupture after bearing of the concrete adjacent to the anchor in the direction of the load (Figures 3-13 and 3-14).

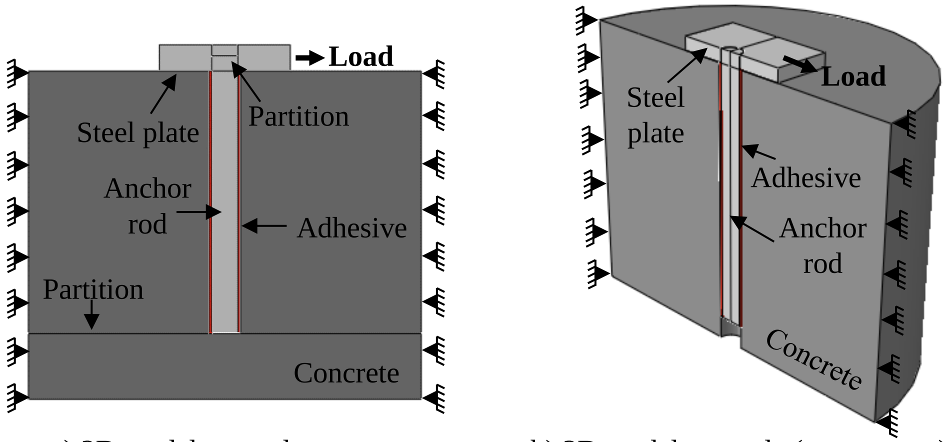

a) 2D model example

b) 3D model example (one-quarter)

Figure 3-12: D20H200 (a) 2D and (b) 3D anchor models for shear loading.

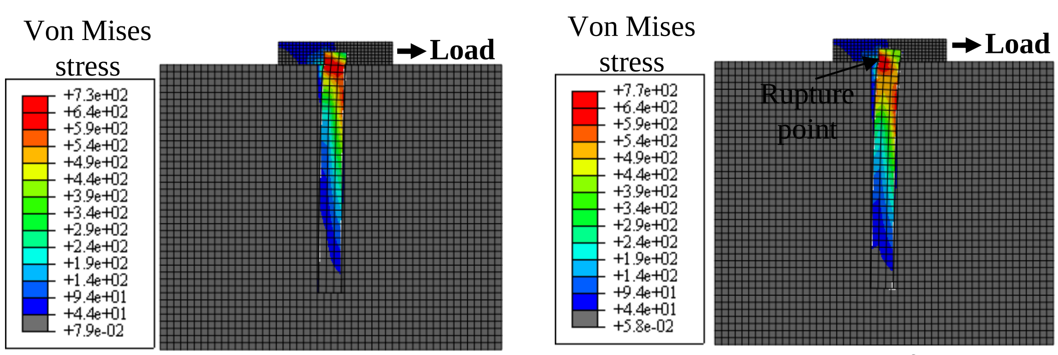

a) Von Mises stress at peak load

b) Von Mises stress at failure

Figure 3-13: D20H200 2D deformed shape and stress at (a) peak load and (b) failure.

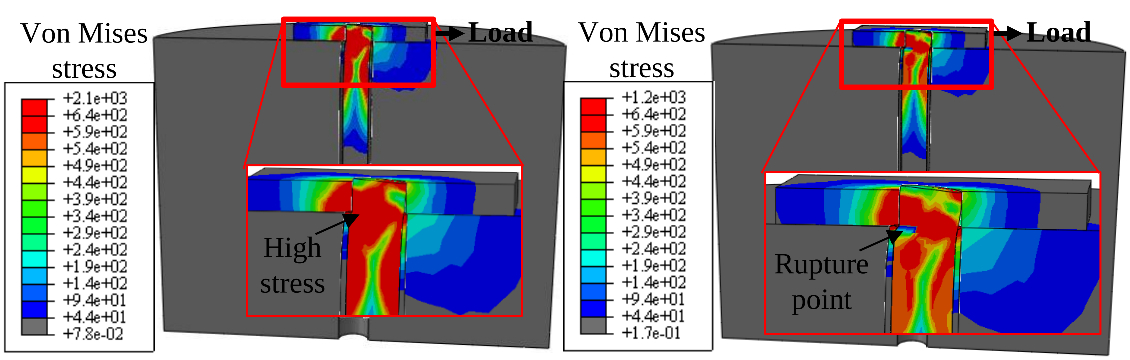

a) Von Mises stress at peak load

b) Von Mises

Figure 3-14: D20H200 3D deformed shape and stress at (a) peak load and (b) failure.

The 2D and 3D models predicted the shear capacity of the anchor well, with approximately the same accuracy (Figure 3-15). Both load-displacement responses were slightly stiffer than the experimental one, but still in reasonable agreement. Therefore, this mechanism was considered verified.

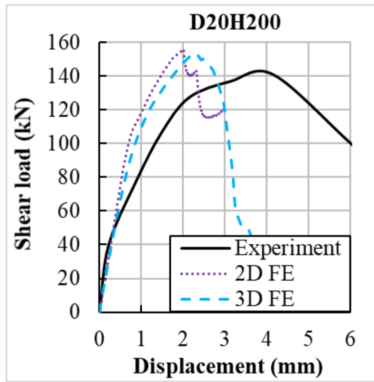

Figure 3-15: Load-displacement curves for steel rupture in shear.

During the verification of the FE approach for static loading, a total of 14 specimens are modeled according to the procedure described above and analyzed under static pullout and shear loading. The numerical-to-experimental load capacity ratios obtained with the 3D models were in the range of ±10% error, as seen in Figure 3-16. Based on these results and on the correct capture of the behaviors expected for each failure mode (discussed above), the FE approach was considered successfully verified.

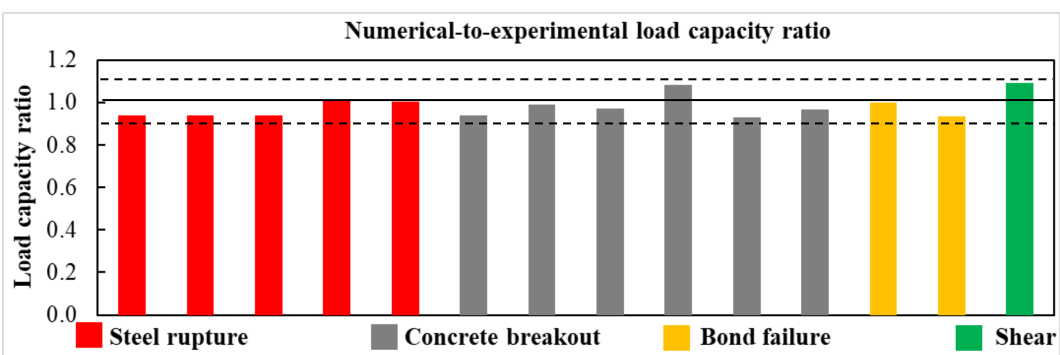

Figure 3-16: Static numerical-to-experimental load capacity ratios.

3.3 Verification of the Finite Element Models for Dynamic Loading

In order to accurately capture the response of the anchors under dynamic wind loads, specimens D16L320W56, D16L80W56, and D20H200 are also analyzed under dynamic pullout loading.

Explicit dynamic analyses are performed using the verified 3D models with the addition of the material densities. Concrete and steel densities are taken as 2.4×10^{-6} and $7.4\times10^{-6}\,kg/mm^3$ respectively, in accordance with typical values. The adhesive density is assumed to be the same as water due to the liquid nature of this material before curing (typical values found range from 1.0×10^{-6} to $1.7\times10^{-6}\,kg/mm^3$). The cyclic behavior of the materials is defined as shown in Figure 3-2. The unloading-reloading stiffness of the concrete and steel are considered the same as their initial tangent stiffness. The adhesive is modeled as holding no residual strain (i.e. the load goes back to zero upon unloading) due to the lack of other material model options for cohesive elements in the FE software.

The load profile is defined according to wind-induced anchor load data published by Erwin et al. (2011), extracted from full-scale experiments on NSC anchorage exposed to strong wind loading. The profile is scaled to 150% the anchor's static capacity (Figure 3-17) to observe their mode of failure under the dynamic loading. This corresponds to 127, 64, and 293 kN for specimens D16L320W56, D16L80W56, and D20H200, respectively.

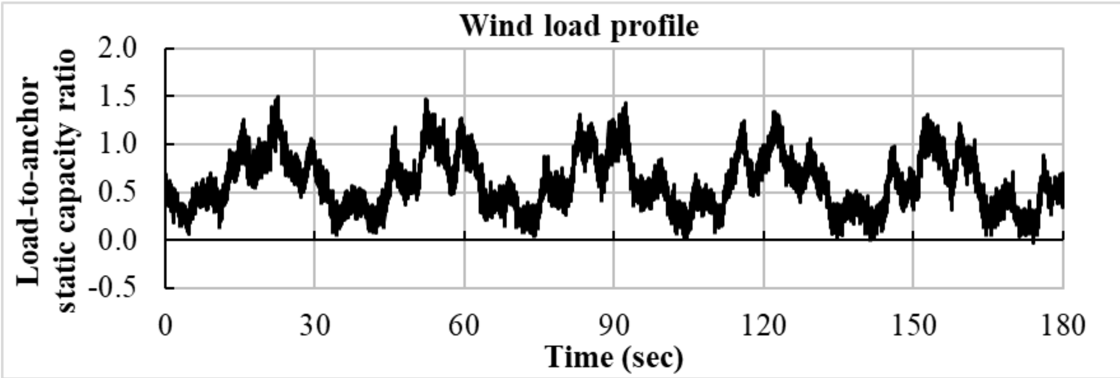

Figure 3-17: Wind load profile applied to single anchors.

In all cases the load and displacement fluctuated following the wind load oscillations until close to 16 sec, when the applied load exceeded the static capacity, resulting in a sudden displacement increase and drop in the reaction, characterizing the failure of the specimens (Figure 3-18). The dynamic load-displacement response was overall slightly stiffer than its static counterpart and reached a higher peak load (Figure 3-18).

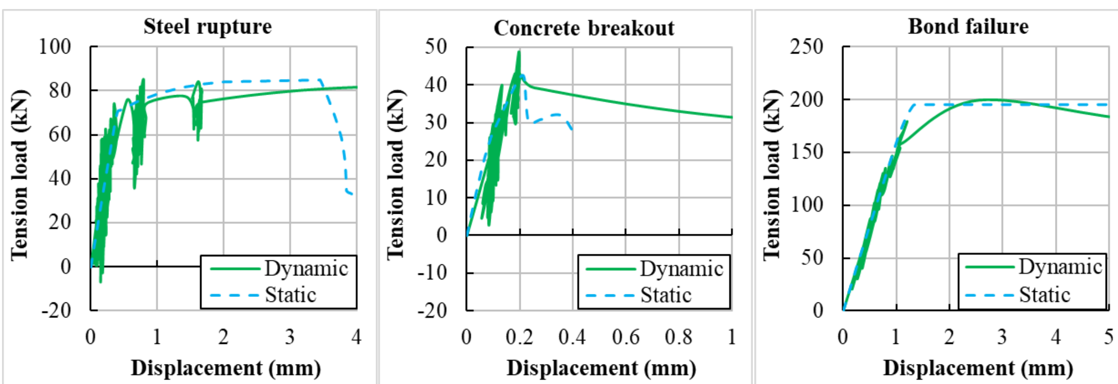

Figure 3-18: Load-displacement curves of the dynamic and static analyses.

A comparison between the load capacity and displacement at peak load from static and dynamic analyses is shown in Table 3.5. The dynamic load capacities were 5 to 15% higher than the static ones. Furthermore, the dynamic response was slightly stiffer in all the cases, as seen in Figure 3-18. These observations agree with experimental results by Hoehler et al. (2011) and Sato et al. (2004). Therefore, the FE approach was considered successfully verified for dynamic loading.

Table 3.5: Summary of load and displacement static and dynamic results.

Specimen	Mode	P_{st} (kN)	δ_{st} (mm)	P_{dyn} (kN)	δ_{dyn} (mm)	P_{dyn}/P_{st}	δ_{dyn}/δ_{st}
D16L160W56	Steel rupture	84.9	3.46	89.1	0.63	1.05	0.18
D16L80W56	Concrete breakout	42.7	0.21	48.9	0.20	1.15	0.93
D20H200	Bond failure	195	1.36	208	1.60	1.02	1.88

3.4 Quantification of the Elevated Temperature and Concrete Cracking Effects

To assess the effect of elevated temperature, specimens D20H200 and D12H70 are analyzed under the temperatures of 38, 60, and 82 °C, reasonable for rooftop applications in the United States. The bond strength and stiffness variations with temperature are defined according to the experimental data published in Lahouar et al. (2017) (Figure 3-19). The temperatures are applied uniformly over the entire model prior to the application of uplift displacement on top of the anchor rod.

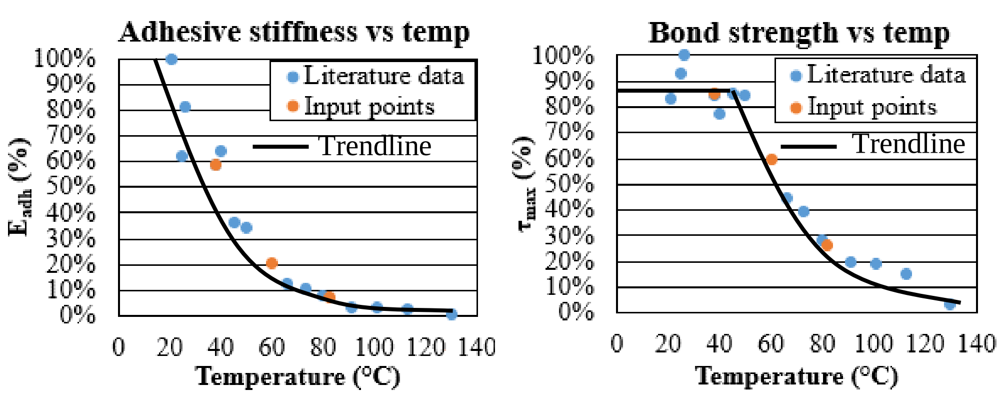

Figure 3-19: Variation of adhesive stiffness and strength with temperature (derived from Lahouar et al., 2017).

The increase in temperature promoted earlier bond failure, with lower stresses created in the concrete (Figure 3-20). It significantly reduced the anchor stiffness and load capacity, reaching a reduction of 70% in the peak load and 86% in the stiffness at 82 °C (Figure 3-21). Thus, this phenomenon can have a considerable contribution to the failure of adhesive anchors installed on a rooftop.

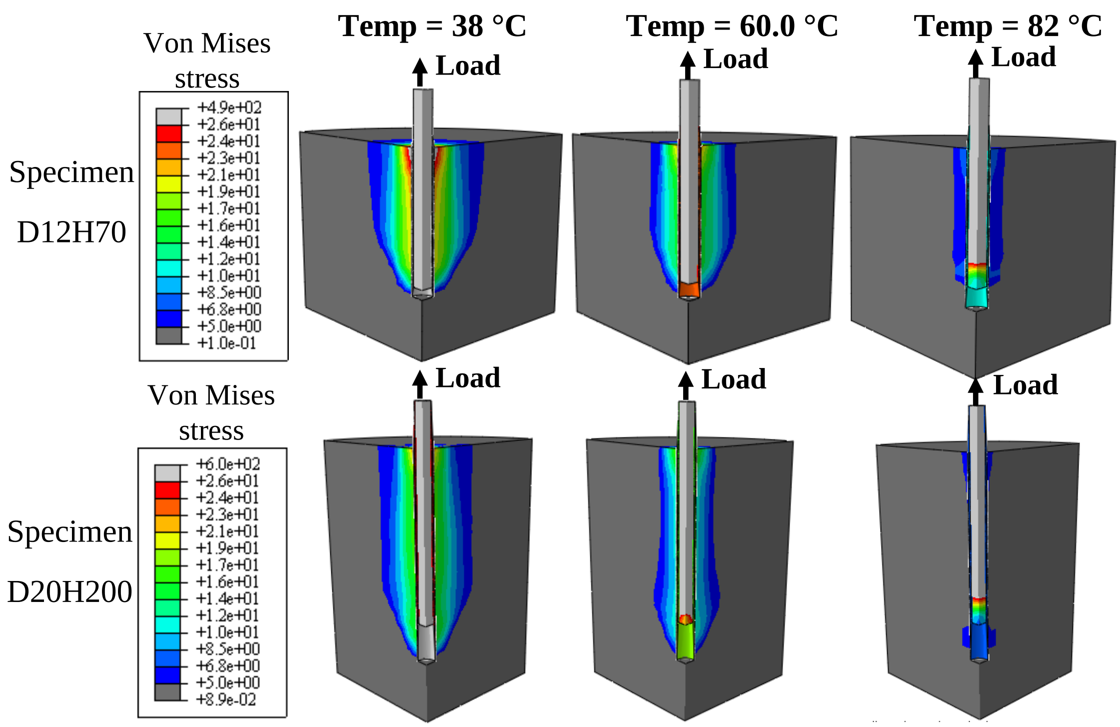

Figure 3-20: Von Mises concrete stress variation with temperature.

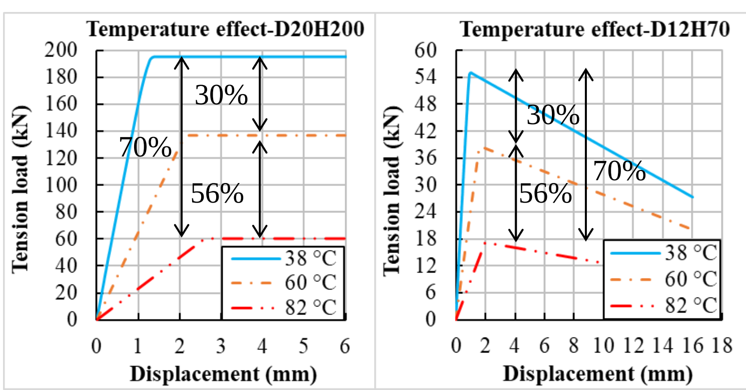

Figure 3-21: Load-displacement response of adhesive anchors at three temperature levels.

Regarding concrete cracking, while its effect on the bond capacity cannot be captured by the FE analysis, it is possible to assess its effect on the concrete breakout response since this mode depends directly on the concrete strength. For that purpose, specimen Ae12 is analyzed in uncracked and cracked concrete. The concrete cracks are formed by applying uniform tensile prestress on the concrete equivalent to its tensile capacity, prior to the application of uplift displacement. The presence of concrete cracking promoted a shallower concrete cone (Figure 3-22a), reduced the concrete stresses (Figure 3-22b), and the breakout load capacity in 20% (Figure 3-23).

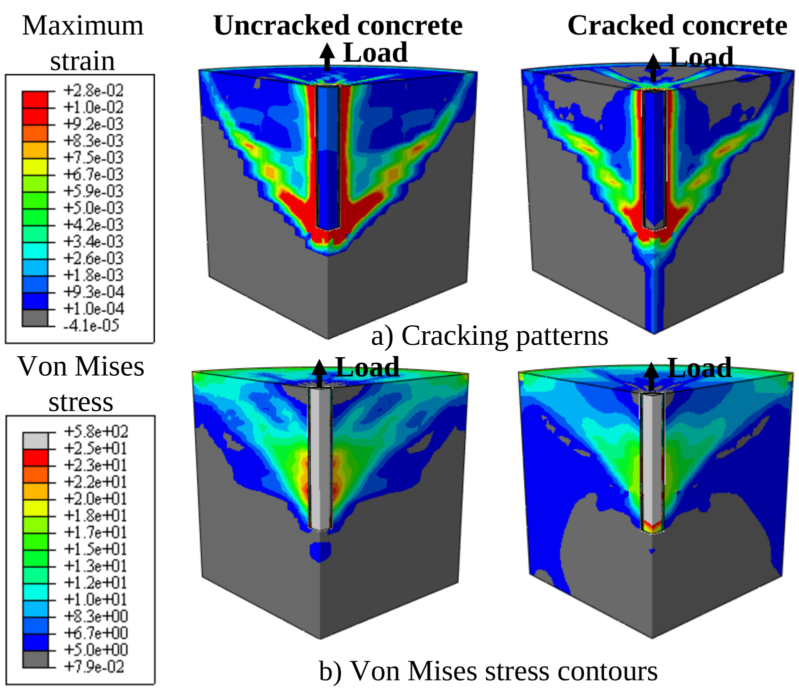

Figure 3-22: (a) Cracking and (b) stress at peak load in uncracked and cracked concrete.

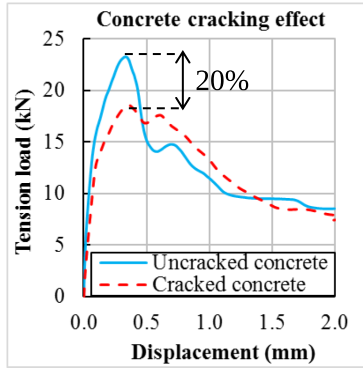

Figure 3-23: Load-displacement response in uncracked and cracked concrete.

The reduction in the concrete breakout load capacity was approximately the same as the reduction in cracked surface area (Table 3.6) suggesting that it is directly proportional to the cracked surface area. This premise is used in Chapter 5 to develop the equivalent cone approach for the assessment of the concrete breakout load capacity using 2D FE models.

Table 3.6: Concrete cracking effect on the concrete breakout capacity and surface area.

Specimen	Concrete condition	θ_{cone}	A_{cone} (mm²)	P (kN)
Ae12	Uncracked	48.5°	12268	22.9
	Cracked	54.3°	10389	18.3
	Ratio cracked/uncracked		**0.85**	**0.80**

3.5 Influence of Key Design Parameters on the Anchor Performance

To evaluate the sensitivity of key design parameters on the anchor response, three of the specimens presenting the failure modes of steel rupture, concrete breakout, and bond failure are selected for a sensitivity study varying embedment depth, anchor diameter, and concrete strength. To facilitate the comparison, the ratio of the maximum to the minimum value of each investigated parameter is 2.0 in all the cases.

As seen in Figure 3-24, the effect of each parameter is specific for each failure mode. The steel rupture capacity is insensitive to the embedment depth (as long as enough embedment is provided to promote this failure mode) but increases quadratically with anchor diameter. On the other hand, the concrete breakout capacity is insensitive to anchor diameter (as long as the anchor diameter is large enough to promote this failure mode) but increases with the embedment depth to a power of approximately 1.7, which is close to the 1.5 power value used by ACI318-14. In addition, the concrete breakout strength increases linearly with the concrete tensile strength but presents little variation with the concrete compressive strength (Figure 3-24c). While these two parameters are strongly correlated in reality, it is possible to isolate their effects and study them independently in FE analysis. Lastly, the bond failure capacity increases linearly with both the embedment depth and anchor diameter at approximately the same rate. Knowing these relationships may be useful in design to avoid overdesigning any parameter and they can be used to define the desired failure mode or choose a combination that will create two simultaneous failure modes, optimizing the use of each material.

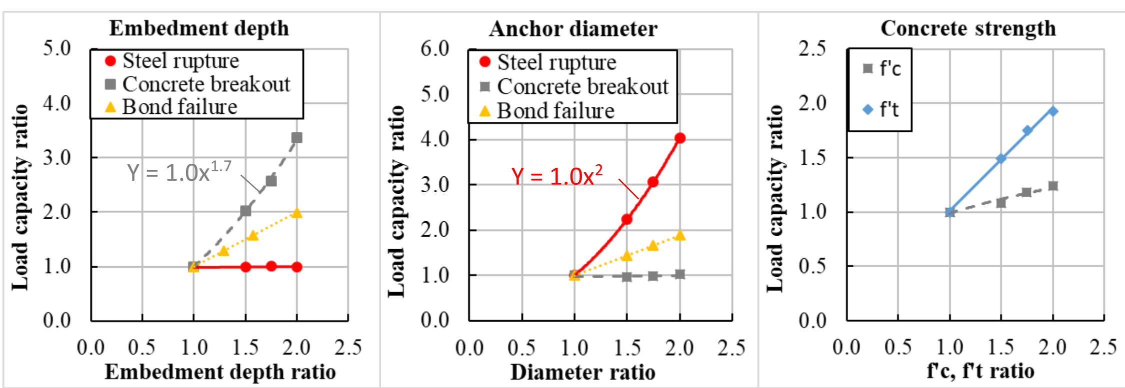

a) Embedment depth influence b) Anchor diameter influence c) Concrete strength influence

Figure 3-24: Sensitivity of the main failure modes to (a) anchor embedment depth, (b) anchor diameter, and (c) concrete strength.

Chapter 4

Holistic NSC-Anchorage Analysis under Strong Wind

The design of NSC anchorage is traditionally done based on experimental results from quasi-static single-anchor tests. This approach neglects the dynamic effect of wind loading and the damaging system-level phenomena such as the bending of the NSC-supporting beams, which can damage the anchors, hence leading to unreliable design.

To assess the system-level windstorm response of an NSC anchored to the rooftop, a holistic FE model of an NSC, its supports, and its anchorage is created using the FE modeling approach verified in Chapter 3. For this analysis, 3D models are used to capture the contact interaction between NSC components and the anchorage. The system is initially analyzed under static pushover to identify its static behavior, including failure mode, load capacity, and load-displacement response. To assess the effect of simultaneous tension and shear action, uplift and lateral loads are applied individually in two separate analyses and then together in a third analysis. Subsequently, the system is analyzed under extreme dynamic wind loading and its behavior is compared to the static response. Lastly, the damage caused by the bending of the NSC-supporting beams on the anchors is investigated for several beam and anchor configurations and new design recommendations are developed to prevent it from promoting premature anchor failure.

4.1 Geometry and Materials Selection

The system consists of a box-shaped NSC, such as an HVAC or converter, supported by two steel W-beams and four anchors at the beam corners. The anchors are installed into an uncracked concrete base representing a rooftop slab with a distance from the edges higher than 1.5 times their embedment depth as recommended by ACI318-14 to permit the full formation of a concrete cone in case concrete breakout governs. The slab has a thickness of 100 mm, which exceeds the anchor embedment depth by more than 67%, also in accordance with ACI318-14, and is supported by 4 steel beams. Only the top flanges of the slab supporting beams are modeled to save computational time.

A 25 x 25 x 130 m (base length x base width x height) building in the risk category II, surface roughness C, and exposure category C according to the definitions of ASCE7-16 is selected for the anchorage design due to its common characteristics, to provide the most applicability. The rooftop NSC dimensions are based on a commercially available HVAC size and defined as 1.24 x 0.83 x 1.31 m (length x width x height).

The NSC anchorage is designed to resist a hurricane category 5 in the Saffir-Simpson scale (maximum wind speed of 70 m/s). The forces on the anchorage are calculated according to ASCE7-16 equations. Based on them, the NSC anchorage is expected to experience a total lateral load of 12.6 kN and a total uplift load of 6.3 kN, when the wind direction is orthogonal to its largest face (i.e. frontal wind), which results in tensile and shear forces on each anchor of magnitude 8.4 and 3.1 kN, respectively.

Based on the design loads, 9.5 mm diameter, 60 mm long anchors (Figure 4-1) are selected from the HIT-RE 100 Hilti catalog (Hilti, 2017) since they are the smallest adhesive anchor able to support the expected tensile and shear loads. These anchors are installed with the HIT-RE 100 adhesive and can resist nominally up to 9.1 kN in tension and 11.2 kN in shear when installed into 27.6 MPa concrete. A thickness of 0.8 mm is selected for the adhesive based on the borehole size recommended by Hilti (2017). M10 hex nuts (Figure 4-1) are selected to connect the anchors to the W-beams as they fit the designed anchor diameter. The anchors are extended 11.2 mm to account for the thickness of the W-beam bottom flange and further 8 mm to accommodate the nuts.

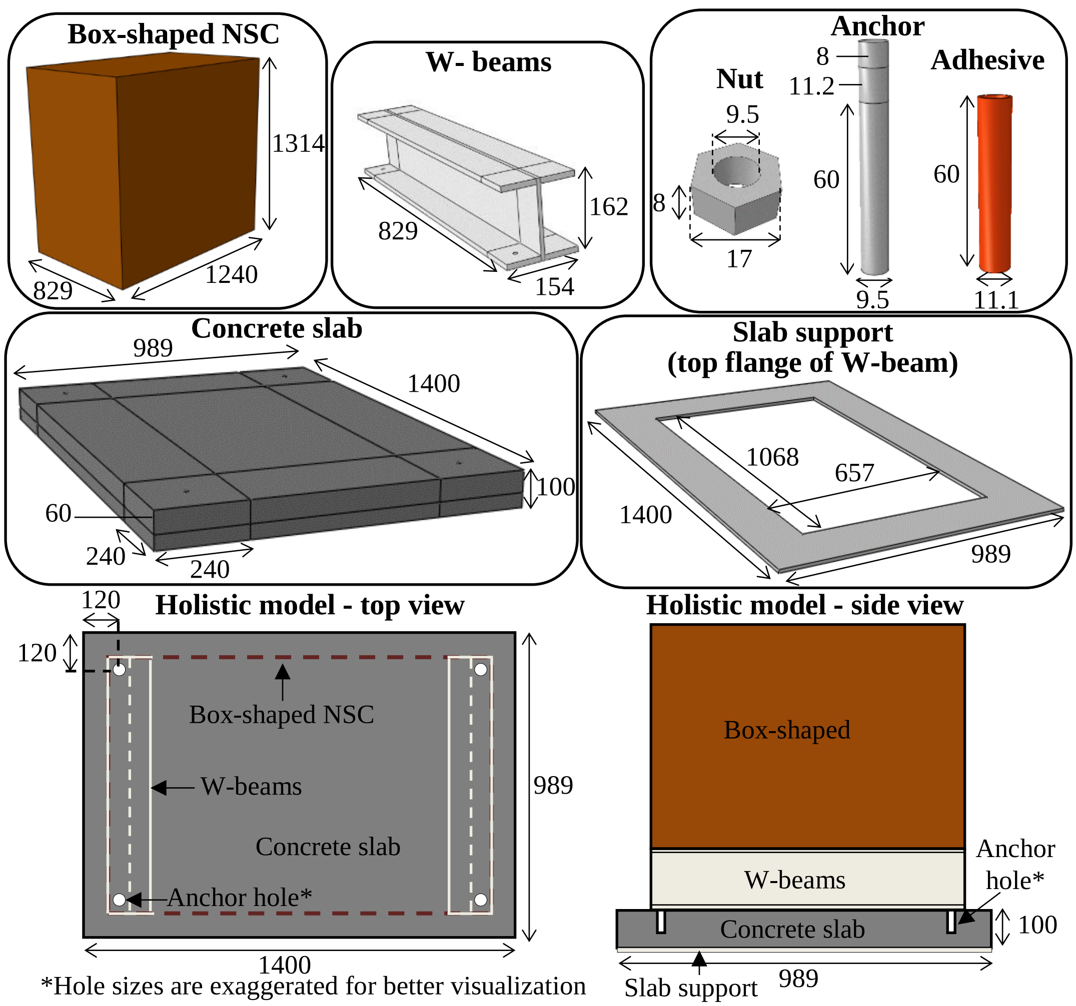

Figure 4-1: NSC-anchorage system components and layout (dimensions in mm).

The NSC-supporting beams are placed in the direction of the wind to better resist the moment caused by it. One anchor is used at the outer ends of each beam, as typically done in construction, totaling four anchors (Figure 4-1). Each anchor is positioned 37 cm away from the center of the W-beam web and 120 mm away from the concrete edges to permit the full development of the concrete breakout capacity. The beam sizes are selected such that the flanges resist the maximum moment caused by the forces on the anchors. W150x150x37.1 steel beam sizes are selected for being one of the most robust (i.e. having short and thick web and flanges) beam options commercially available in order to prevent excessive bending of the beam that would damage the anchors. The selected concrete slab size is 989 x 1400 x 100 mm in width, length, and height, respectively (Figure 4-1), to comply with the NSC dimensions and the minimum concrete thickness specified in Hilti (2017).

The concrete compressive strength is defined in accordance with the anchor selection as 27.6 MPa. Its tangent elastic modulus and tensile strength are calculated as 24,692 MPa and 1.73 MPa using Eqs. 3.1 and 3.2, respectively. The adhesive strength is calculated to provide the anchor design load capacity in tension as 4.35 MPa based on the uniform bond model, as per Eq. 4.1.

$$\tau_{\max} = \frac{P_{\max}}{\pi d_a h_{ef}} \qquad (4.1)$$

Where:

$\tau_{\max}$ = Maximum bond stress

$P_{\max}$ = Maximum bond load capacity

d_a = Anchor diameter

h_{ef} = Anchor embedment depth

4.2 Holistic Analysis Approach

During the FE modeling, the NSC is fixed to the W-beams, which in turn has normal contact with the bottom of the nuts and the sides of the anchors. Each anchor is bonded via its adhesive to the concrete slab, which is fixed to its supporting beams. The NSC, W-beams, and slab supports are modeled as linear-elastic to save computational resources since they are not expected to experience high stress. The steel anchor, concrete, and adhesive material models are created following the approach described in Chapter 3. The adhesive behavior is defined as elastic-plastic due to the lack of post-peak data provided by the manufacturer.

A force-controlled analysis is chosen to ensure the appropriate uplift-to-lateral pressure ratio. Furthermore, the application of lateral pressure generates moment on the system, in contrast with the application of uniform lateral displacement over the NSC surface. The downside of this option is that the post-peak behavior is not observed (i.e. the analysis only runs up to failure).

To understand the effect of each wind load component, the NSC-anchorage system is initially analyzed under uplift loading only, then under lateral pressure only, and finally under both uplift and lateral loading.

To analyze the behavior of the system under uplift only, upwards pressure is applied at the top of the NSC, whereas under lateral loads positive and negative pressures are applied at the front and back faces (largest sides) of the NSC. The combined load case simply consists of both uplift and lateral loads applied together (Figure 4-2). The boundary conditions consist of fixing the bottom of the concrete slab support, which is perfectly bonded to the bottom of the concrete (Figure 4-2).

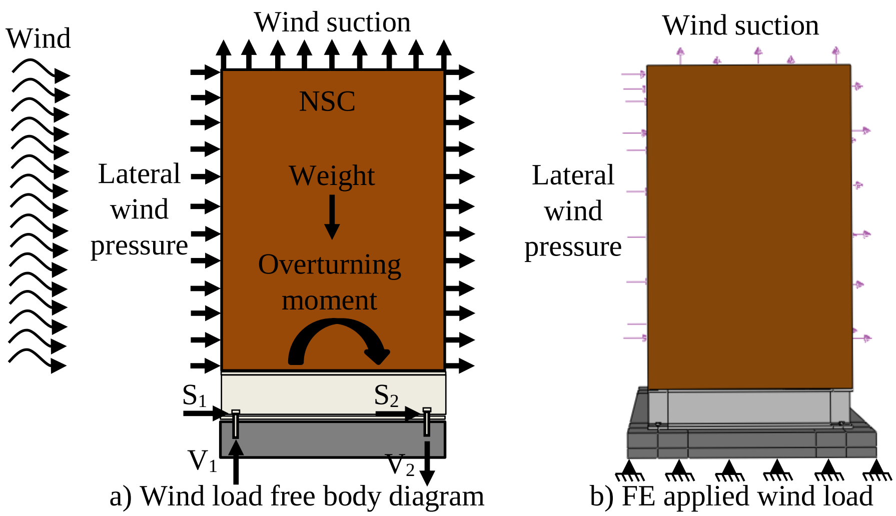

Figure 4-2: Simultaneous uplift and lateral load application and boundary conditions.

4.3 NSC Anchorage Discrete Analysis

To provide a reference for the expected system behavior and confirm that the anchors reached their design capacities, a single adhesive anchor with the geometry and properties described above is modeled and analyzed under static tension and shear. A piece of the W-beam's bottom flange is also modeled to perform the shear analysis, as well as the nut. A displacement-controlled analysis is preferred in both cases (Figure 4-3) since it can capture the post-peak response and no significant moment is expected during shear loading due to the low distance from the load applied to the concrete slab.

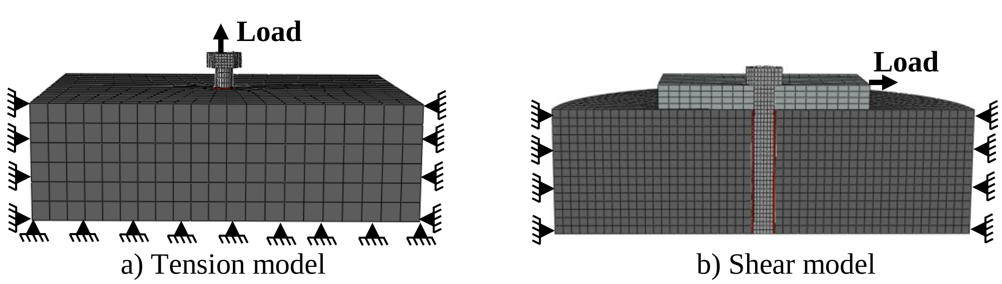

Figure 4-3: Single-anchor model and load application in (a) tension and (b) shear.

Under static tensile load, the anchor presented bond failure and was pulled out with little concrete engagement and no yielding of the steel (Figure 4-4). Under static shear load, bearing of the concrete was initially observed adjacent to the anchor, followed by rupture of the steel rod. The steel rupture occurred at the contact of the bottom of the steel plate with the anchor rod (Figure 4-5).

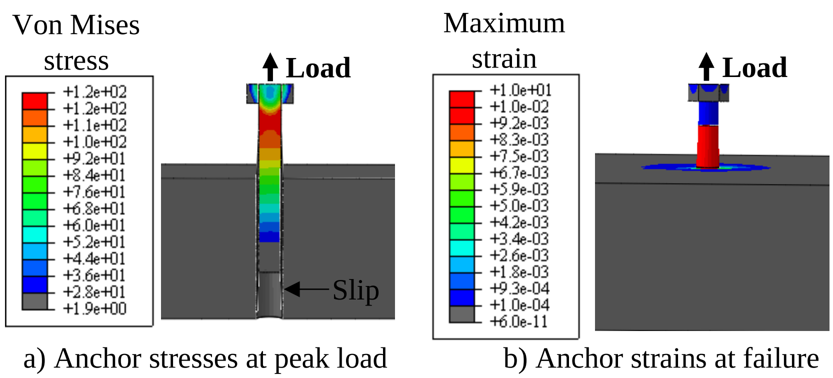

Figure 4-4: Anchor stress under tension loading at (a) peak load and (b) failure.

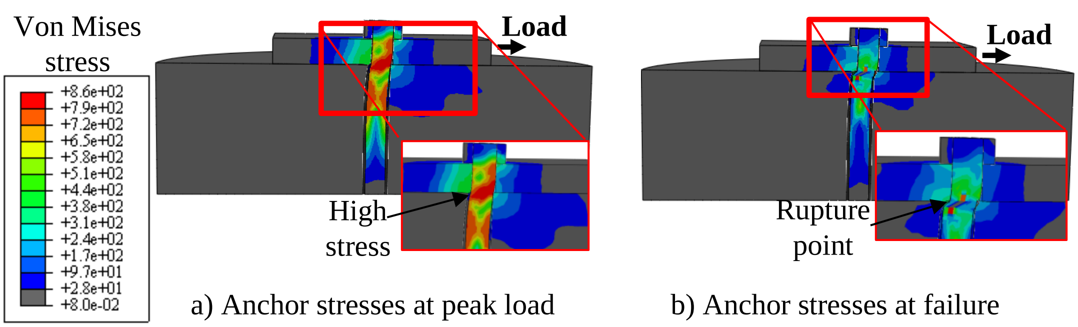

Figure 4-5: Anchor stress under shear loading at (a) peak load and (b) failure.

Under static pullout loading, bond failure was observed at a peak load of 8.4 kN and after an initial linear branch with a stiffness of 54 kN/mm (Figure 4-6), with little engagement of the concrete and the steel stresses remaining around 25% of its yielding strength. This is sufficient to meet design expectations. Under static shear loading, the anchor load-displacement response was nonlinear, with failure due to rupture of the steel at a peak load of 38.5 kN (Figure 4-6), considerably above the design needs. Therefore, the anchor model was considered satisfactory for the design loading.

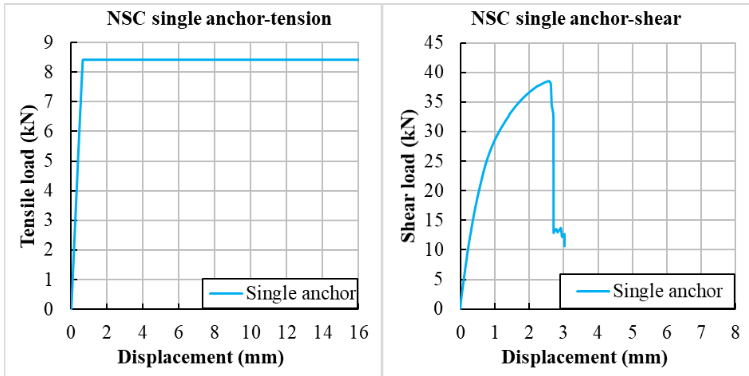

Figure 4-6: Single-anchor load-displacement response under static tension and shear.

4.4 NSC-Anchorage Holistic Static Analysis

Wind loads create simultaneous lateral and uplift loads that result in tension/compression and shear on the anchorage (Figure 4-2a). To understand the effect of simultaneous tension and shear action, the system is initially analyzed under uplift only, then a second analyzed is performed applying lateral pressure only, and finally, a third analysis is performed applying both lateral and uplift loading. The lateral pressure is applied to the largest NSC surface to represent frontal wind, which is the critical case.

Under only uplift, the NSC moved up, pulling its supporting beams and the anchorage (Figure 4-7). As all anchors were equally pulled out, the adhesive elongated steadily until their capacity was reached in bond failure (Figure 4-8) at 33.6 kN, which corresponds to the full pullout capacity of the four anchors. In addition, the web of the W-beams bent significantly, despite their robust geometry and linear-elastic material behavior (Figure 4-7). This bending created higher stresses on the anchors but was not enough to promote their premature failure in steel rupture in this particular case. However, this effect is expected to be significant in typical NSC connections since the W-beam size selected was among the most robust (i.e. having short and thick web and flanges) found. A detailed investigation of this phenomenon is performed and the results are discussed in Section 4.6 of this chapter.

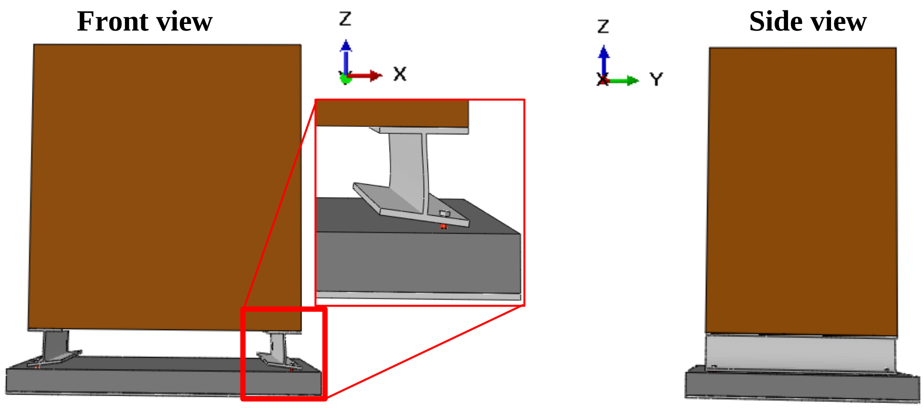

Figure 4-7: NSC-anchorage system deformed shape under static uplift.

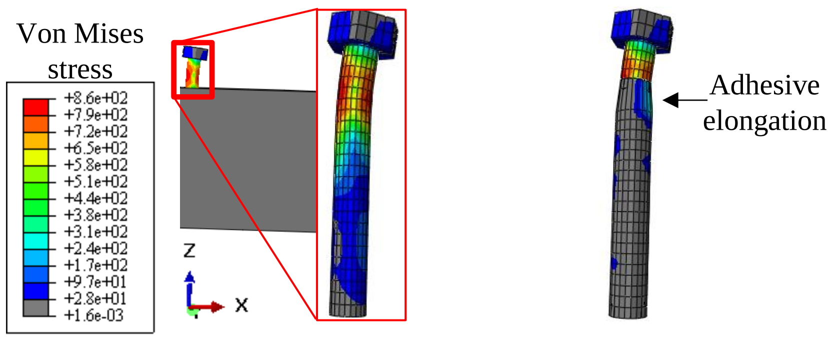

a) Anchor stress at peak load b) Adhesive elongation at failure

Figure 4-8: (a) Anchor stress and (b) adhesive elongation under NSC static uplift.

Under only lateral pressure the NSC was observed to tip along the direction of the loading due to the overturning moment created by the load, causing the two anchors on the leeward side to be pulled out whereas the windward side experienced compression (Figure 4-9). The anchors in tension were critical and presented bond failure (Figure 4-10), while the anchors on the compression side were not significantly affected as the W-beams provided most of the load when compressed against the concrete slab, which can be confirmed by noting that the concrete stresses under the W-beams were significantly higher than under the anchors (Figure 4-11). The lateral capacity of the system in this scenario was 17 kN, which is slightly superior to the capacity of the two anchors on the tension side. The concrete did not experience significant stresses or deformation.

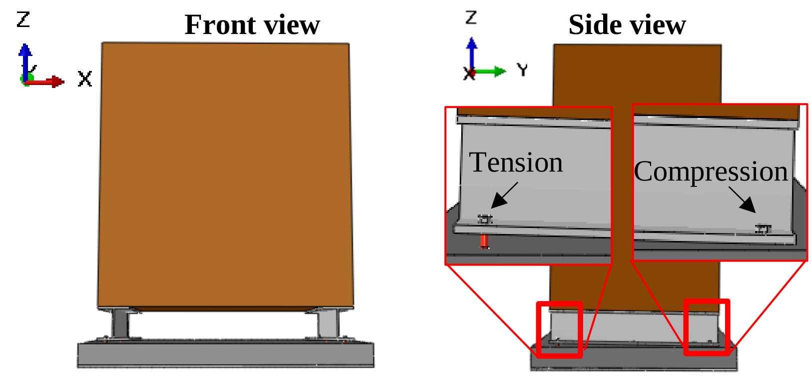

Figure 4-9: Full system deformed shape under static lateral load.

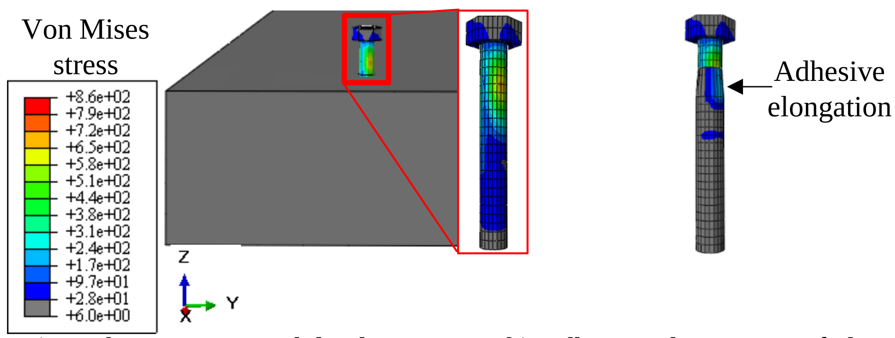

a) Anchor stress at peak load

b) Adhesive elongation at failure

Figure 4-10: (a) Anchor stress and (b) adhesive elongation under NSC static lateral load.

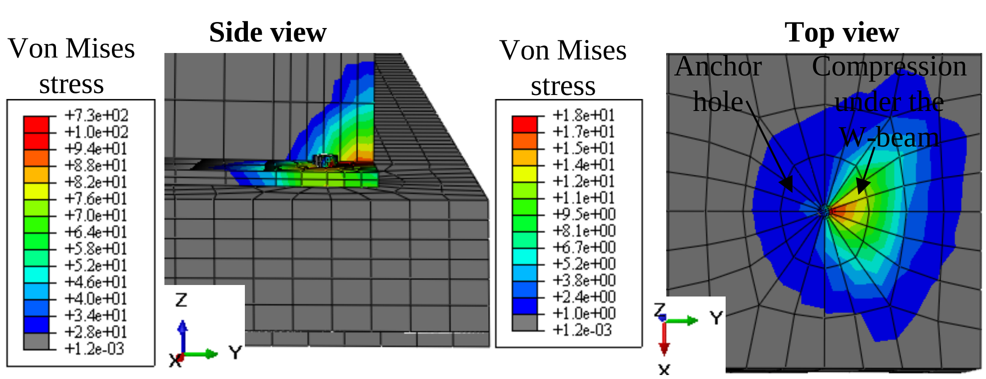

Figure 4-11: Stresses in the W-beam and concrete in the compression zone.

Under both uplift and lateral pressure, the system presented a similar behavior as when it was analyzed under lateral pressure only (Figures 4-12 and 4-13), with the two anchors on the leeward side being pulled out in tension and experiencing bond failure and the W-beams on the windward side being compressed against the concrete slab. The stresses in the anchors under compression remained below yielding until after the peak load and the adhesive around them did not deform significantly, again due to the W-beams picking up most of the load in the region. The system's lateral capacity was 14.5 kN, which is 15% lower than under lateral pressure only. This reduction in load capacity is attributed to the simultaneous action of tension and shear forces on the anchors.

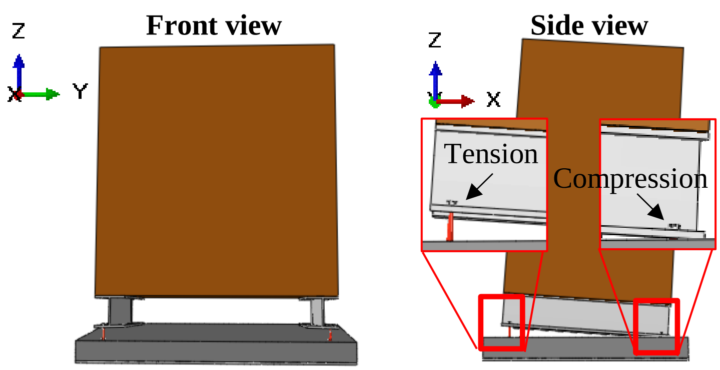

Figure 4-12: NSC-anchorage system deformed shape under static uplift and shear.

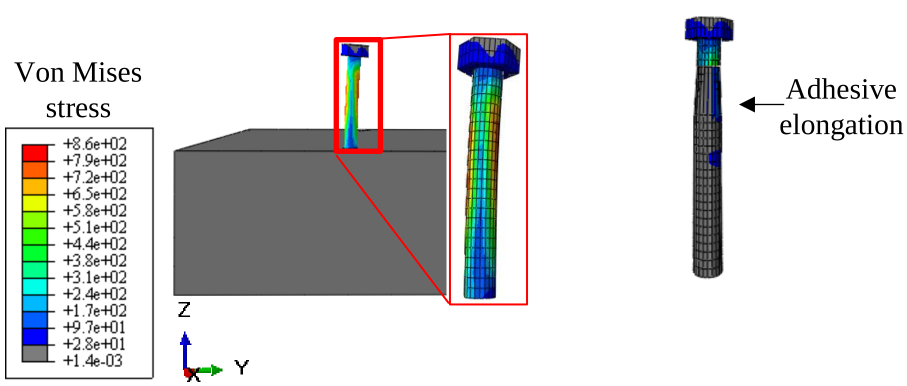

a) Anchor stress at peak load b) Adhesive elongation at failure

Figure 4-13: (a) Anchor stress and (b) adhesive elongation under tension and shear.

4.5 NSC-Anchorage Holistic Dynamic Analysis

Although static approximations of the wind loads are used for design, in reality, these loads are highly dynamic. To simulate this condition realistically, an explicit dynamic analysis of the NSC-anchorage system is performed. The system is subjected to dynamic wind loading corresponding to a hurricane category 5 in the Saffir-Simpson scale. The load versus time profile is defined according to full-scale experiments performed by Erwin et al. (2011). They measured the wind pressure on small HVAC units under a wind of 38 m/s (85 m.p.h.) maximum speed. To adjust the load to the NSC studied, the profile is multiplied by the ratio of the frontal and top surface areas of the analyzed NSC to the tested HVAC, which was $\frac{1.24\times 1.13}{0.9\times 0.5}=3.11$ for the lateral pressure and $\frac{1.24\times 0.83}{0.9\times 0.7}=1.63$ for the uplift. In addition, to simulate a hurricane category 5 with a maximum wind speed of 70 m/s (157 m.p.h), the load is also multiplied by $\left(\frac{70}{38}\right)^2$ since the wind pressure is known to increase with the square of its velocity. Finally, the load is multiplied by 2.6 to allow the failure of the system to be observed. After these adjustments, the final load profile used in this study is obtained as shown in Figure 4-14.

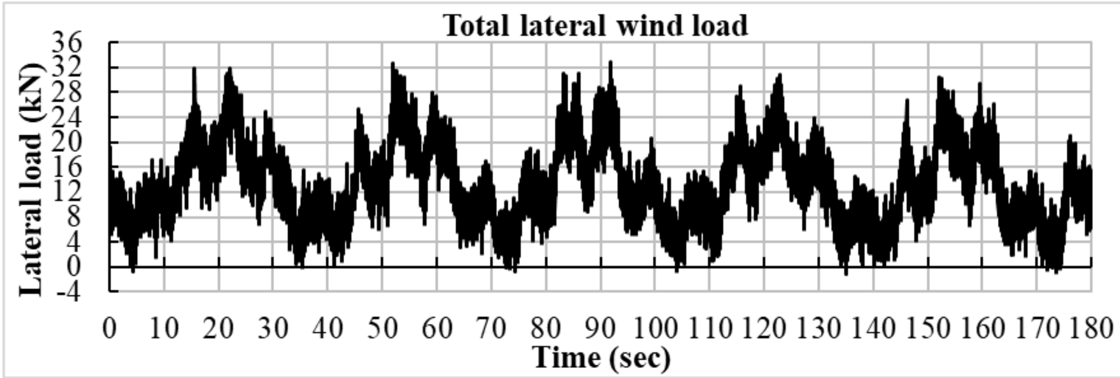

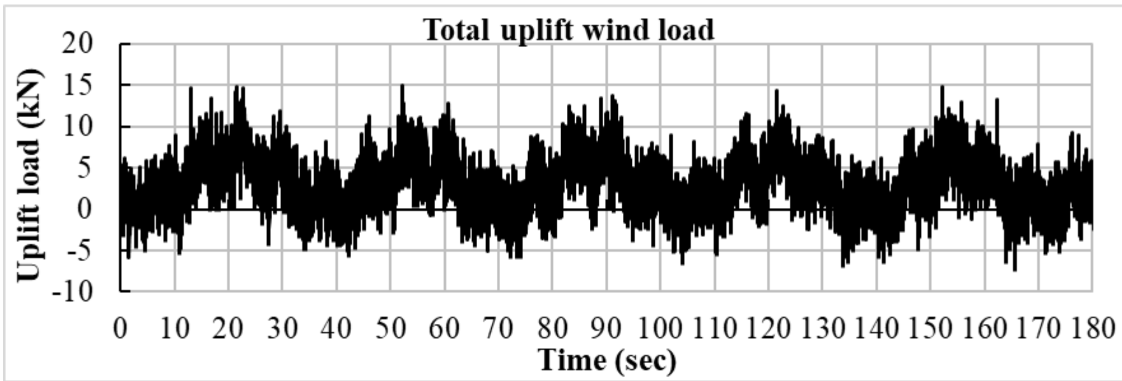

Figure 4-14: Applied wind load profile, adapted from Erwin et al. (2011).

Under dynamic loading the system moved back and forth in the direction of the wind, never returning to its original position. This is due to the wind load acting predominantly in the same direction. In addition, the system experienced a top average velocity of 6 mm/s and acceleration of 25 mm/s², which occurred near failure and at the beginning of the load application respectively.

During this analysis, the system gradually accumulated displacement, eventually failing after approximately 10 seconds of load application at 16 kN of lateral load (Figure 4-15), which is 10% greater than its static capacity (Table 4.1). This suggests that dynamic analyses are not necessary since the static loading case is more critical. However, the dynamic analysis also showed that the NSC anchorage accumulated significant inelastic displacement before failure, which is not considered in design provisions and could cause damage to the system, compromising the NSC operation. Therefore, a displacement check is advised in the design of NSC anchorage.

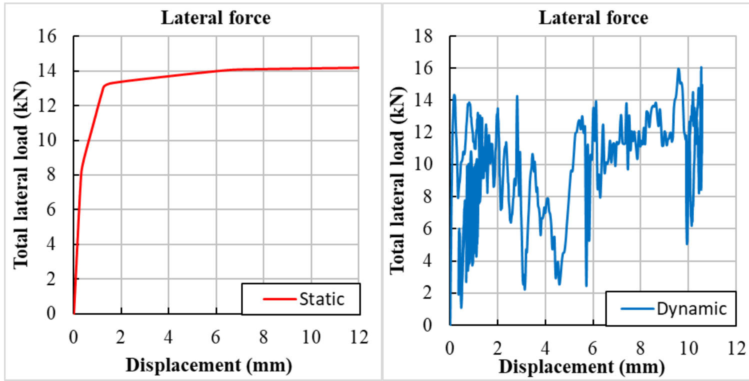

Figure 4-15: NSC static and dynamic responses of the under strong wind.

Table 4.1: Static and dynamic load capacities and displacements at peak load.

Analysis type	Vertical reaction	Lateral reaction	Vertical displacement	Lateral displacement
	kN	kN	mm	mm
Static analysis	5.7	14.5	1.00	1.30
Dynamic analysis	8.1	16.1	0.07	0.16
Dynamic/Static	1.4	1.1	0.07	0.15

4.6 Bending of the NSC-Supporting Beams

During the holistic analyses, significant bending of the NSC-supporting beams was observed when lateral pressure was applied (Figure 4-16a). The leeward wind pressure caused the web of the W-beams to bend significantly in the direction orthogonal to the wind, which created additional stresses on the sides of the anchors at their points of contact with the beam (Figure 4-16b), damaging the anchors. To investigate this phenomenon and quantify this damage, a sensitivity study is performed varying the thickness of the web and bottom flange of the beam and the distance from the center of the anchor to the center of the beam web, hereon after called “eccentricity” distance (Figure 4-16). For that purpose, FE models of the NSC W-beams anchored to the concrete slab are created and analyzed by applying uplift displacement on top of the W-beam.

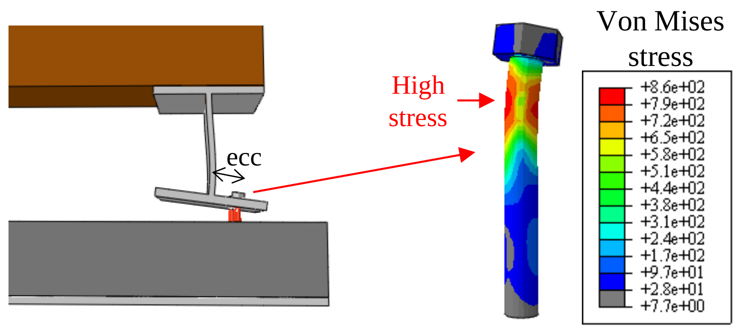

a) Bending of the NSC-supporting beam b) High anchor stress

Figure 4-16: (a) Bending of the NSC-supporting beams and resulting (b) anchor stress.

First, the eccentricity distance (*ecc*) is varied from 0 to 67 mm, which was the maximum permissible by the W-beam's bottom flange width. The W-beam web and bottom flange thicknesses are kept as 8.1 mm and 11.6 mm, respectively. Bond failure of the anchorage at its full capacity (8.4 kN) was observed for eccentricity values below 47 mm. Above that distance, steel rupture of the anchor rod was prematurely caused by the additional stresses promoted by the bending of the W-beam's web and reducing the anchor load capacity linearly with the increase in eccentricity (Figure 4-17a). This is attributed to the linear increase in moment created around the web as the eccentricity increased. The eccentricity distance at which the failure mode changes and the load capacity consequently reduces was named "critical eccentricity". It is noted that the critical eccentricities obtained were within half of the length of the W-beam's bottom flange, therefore the premature steel rupture may govern in practical applications.

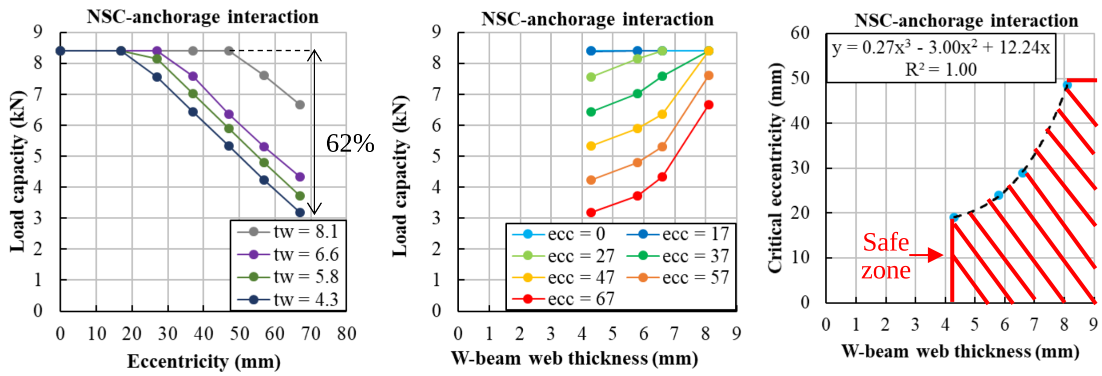

a) Influence of eccentricity b) Influence of web thickness c) Critical eccentricity

Figure 4-17: Influence of the (a) eccentricity and (b) beam web thickness on the bending of NSC-supporting beams and (c) critical eccentricity variation.

Second, the previous analyses are repeated for the same range of eccentricity distances but varying the beam web thickness (t_w) from 4.3 to 8.1 mm, which are typical dimensions of these types of beams. The reduction in web thickness caused a reduction in load capacity to the cubic power (Figure 4-17b), which is attributed to the relationship between the web's second moment of inertia (related to the cube web thickness) and its bending. It also implies that this parameter is more significant than the eccentricity. In the most severe case, a reduction of 62% of the anchor load capacity was observed.

Lastly, the thickness of the bottom flange of the W-beam is varied from 5.6 to 41.6 mm, which are typically commercially available dimensions. The anchor response was insensitive to this change, keeping a bond failure at the anchor load capacity of 8.4 kN. This is consistent with the observations from the NSC-anchorage system response since the bottom flange of the W-beams did not experience significant bending themselves. Even the lowest flange thickness investigated did not bend significantly.

To provide new design recommendations on how to avoid the premature steel failure in NSC anchorage, the variation of the critical eccentricity distance with the W-beam web thickness is plotted and best fitted by a cubic function with a set intercept in the origin (Figure 4-17c). In order to avoid premature steel failure of the NSC anchorage, it is advised that the web thickness and eccentricity distance be selected so that they remain below and to the right of the curve plotted in Figure 4-17c, respectively. Due to their similarity with the W-beam shape, this recommendation is expected to apply to C channels as well.

Chapter 5

Equivalent Cone Approach

During the finite element analysis of anchors, 3D models are typically used to capture the three-dimensional distribution of stresses and strains caused by pullout loading. This becomes important in the concrete breakout failure mode, in which the 3D strain distribution governs. Conversely, the use of 2D FE models is simpler and faster as the geometry can be more easily created in the model and the analysis time is shorter due to the lower number of degrees of freedom in these models, which also reduces their computational demand. Therefore, the use of 2D FE models for the numerical analysis of anchors is highly desired. In this chapter, a so-called "equivalent cone" approach is developed to permit the use of 2D FE models to accurately predict the anchor load capacity under static pullout loading in all the main failure modes (presented in Chapter 3).

One of the challenges in the creation of a 2D FE anchor model lies in the definition of the concrete thickness. While 2D models can accurately predict the anchor load capacity in the failure modes of steel rupture in tension and bond failure, as shown in Chapter 3, to accurately predict their load capacity in the concrete breakout failure mode the thickness of the concrete must be properly defined. Unlike 3D models, 2D models do not capture the three-dimensional stress distribution in the concrete breakout mode, but instead, consider a uniform stress distribution through the entire thickness of the elements. Therefore, inputting the thickness of a concrete slab, for example, would greatly overestimate the concrete breakout capacity. With that in mind and building on the idea that the concrete breakout capacity is proportional to the cracked surface area, developed in Chapter 3, the equivalent cone approach is developed to define an equivalent concrete thickness that accurately predicts the anchor load capacity in concrete breakout. The approach is based on the following premises:

- The concrete breakout manifests in a conical shape in 3D models and experiments.
- The concrete breakout load capacity is proportional to the cracked surface area.
- The angle of the concrete cone can be approximated by the 2D cracking angle.
- The load capacity of the 2D FE model varies linearly with the beam thickness.

The first premise is verified by the results presented in Chapter 3 when specimens presenting the concrete breakout mode were analyzed. The second premise is evidenced by the concrete cracking study in Section 3.5 of Chapter 3 and is further supported by the results given in section 5.1 along with the third premise. The fourth premise is confirmed by a parametric study varying the thickness of the concrete in specimen D45H150 from 50 to 500 mm, shown in Figure 5-1.

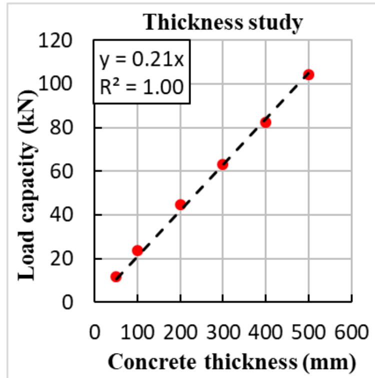

Figure 5-1: Variation of the concrete breakout capacity with the concrete thickness.

Based on these premises, it is possible to calculate the concrete thickness in a 2D model that will equal the cracking area, which consists of a trapezoidal shape, to the three-dimensional concrete cone surface area, which consists of a conical shape (Figure 5-2). This can be done according to Eqs. 5.1 to 5.5, as shown in the flowchart in Figure 5-3.

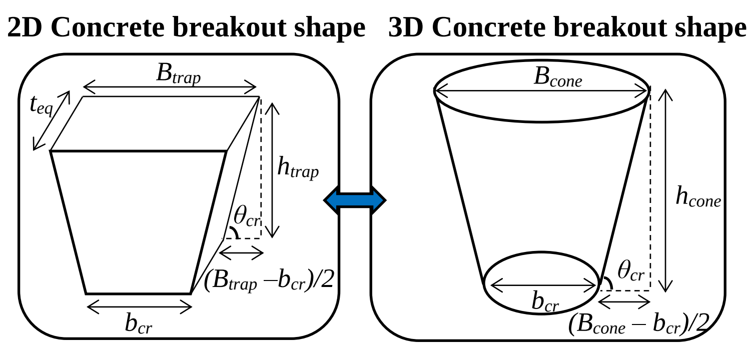

Figure 5-2: 2D and 3D concrete breakout shapes.

$$B_{cone} = b_{cr} + \frac{2h_{cone}}{\tan(\theta_{cr})} \tag{5.1}$$

$$As_{cone} = \frac{1}{2}\pi h_{cone}(B_{cone} + b_{cr}) \tag{5.2}$$

$$B_{trap} = b_{cr} + \frac{2h_{trap}}{\tan(\theta_{cr})} \tag{5.3}$$

$$As_{trap} = \left(2\sqrt{\left(\frac{B_{trap} - b_{cr}}{2} \right)^2 + \left(h_{trap} \right)^2} \right) t_{ini} \qquad (5.4)$$

$$t_{eq} = t_{ini} \frac{As_{cone}}{As_{trap}} \qquad (5.5)$$

Where:

b_{cr} = Base of the cracked trapezoidal and cone shapes

θ_{cr} = Angle of the cracked trapezoidal and cone shapes

B_{cone} = Base of the cracked cone shape (3D)

B_{trap} = Base of the cracked trapezoidal shape (2D)

h_{cone} = Height of the cracked cone shape (3D)

h_{trap} = Height of the cracked trapezoidal shape (2D)

As_{cone} = Surface area of the cracked cone shape (3D)

As_{trap} = Surface area of the cracked trapezoidal shape (2D)

t_{eq} = Equivalent concrete beam thickness

t_{ini} = Initial concrete beam thickness (estimated)

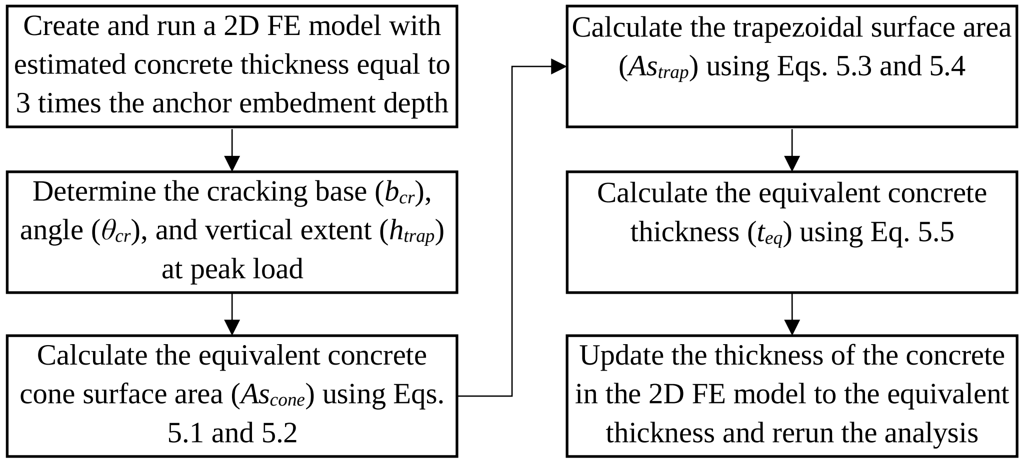

Figure 5-3: Equivalent cone approach flowchart.

In the procedure described in Figure 5-3, the initial thickness (t_{ini}) is estimated based on the concrete breakout area adopted in ACI318-14 provisions, which consists of a square with side size equal to three times the anchor embedment depth. The cracking base (b_{cr}) and height of the cone shape (h_{cone}) are considered equal to the anchor tip diameter and embedment depth, respectively. The vertical crack extent (h_{trap}) and angle (θ_{cr}) are the height of the major crack and crack angle with the horizontal observed when the anchor reaches its load capacity (i.e. peak load) in the FE model. Since direct visualization of the cracks is not provided by the FE platform used, cracks are determined as the areas where the concrete strain exceeds the cracking strain defined in the concrete tensile behavior. Application of the approach requires the use of an initial model in the first step, which is updated in the last step. By following this approach, the concrete breakout capacity of single anchors is accurately predicted by 2D FE models, as shown in Section 5.1.

5.1 Verification of the Equivalent Cone Approach

To verify the equivalent cone approach, it is applied to the six anchor specimens verified in Chapter 3 (Table 3-1) that present concrete breakout. 2D FE models of the specimens were created with the concrete thickness defined as described in Figure 5-3 and analyzed under static pullout. The cracking angle obtained from 2D models is compared to the one observed in the 3D models and the load capacity obtained with the 2D models is compared to the experimental load capacity.

The cracking angle predicted in the 2D models was shown to be a good approximation to the concrete cone angle predicted by 3D models, as exemplified in Figure 5-4, in agreement with the third premise in the above section. Furthermore, the load capacities obtained with this approach were in good agreement with experimental results, staying within ±10% error (Figure 5-5). Therefore, the equivalent cone approach was considered verified.

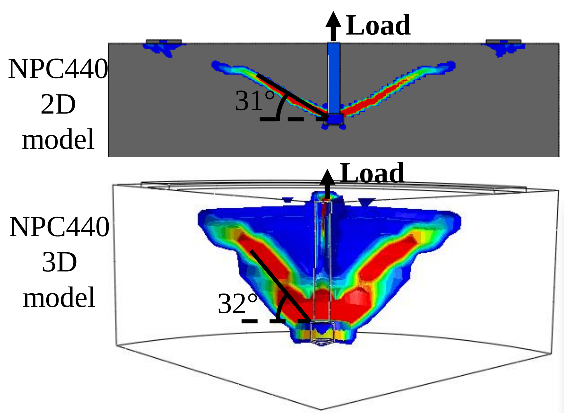

Figure 5-4: Comparison between the cracking angle predicted by the 2D and 3D models.

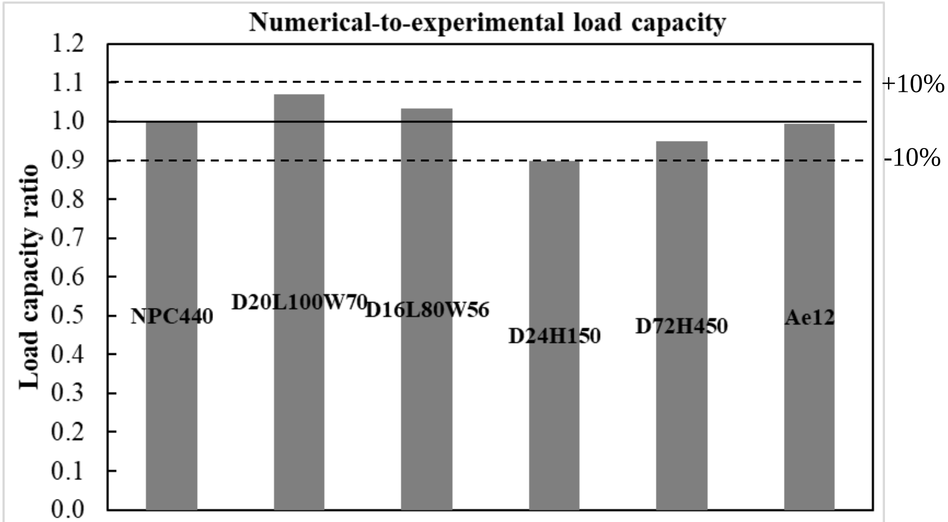

Figure 5-5: Comparison of the load capacity predictions from the 2D models and experiments.

To allow fast and easy use of this approach by researchers and engineers, an open-access spreadsheet was programmed with the procedure in Figure 5-3 and made available at A. Almeida Jr. and Guner (2019b).

Chapter 6

Artificial Neural Network

Finite element models are a valuable tool when a detailed understanding of the anchor behavior is desired. However, they require a high level of expertise to be created correctly, usually take significant time to develop the model and run the analysis (up to several hours, depending on the complexity of the problem), and may not capture all relevant phenomena. For example, they do not capture the degrading effect of concrete cracks on the bond between the resin of adhesive anchors and the concrete. Therefore, an alternative method is needed to predict the capacity of adhesive anchors damaged by concrete cracking.

In those situations, artificial neural networks (ANN) can be an alternative solution. ANNs can be used to predict the anchor capacity within seconds given basic input only, being more appropriate for design or strength assessment when a faster and simplified analysis is desired and typically only the load capacity or displacement are sought. ANNs have been used for anchor applications in uncracked concrete (e.g. Gesoglu et al., 2014; Gesoglu and Guneyisi, 2007; Ashour and Alquedra, 2005; Sakla and Ashour, 2005), however, specimens damaged by concrete cracking have never been considered.

An ANN is an artificial intelligence-based computational model with the ability to "learn", in the sense of recognizing patterns and adapting to them to achieve the desired output (e.g. load capacity). The output is typically obtained in a short time (e.g. within seconds) and using the ANN can be considered easy.

The network is composed of several highly-interconnected artificial neurons organized in layers that communicate with the previous and the next ones (Figure 6-1). The neurons in the first layer receive the input signal, modify it, and pass it to the neurons in the next layer, in a process called "forward propagation". Modification of the input (x) is performed according to weights (w) and biases (b) associated to each neuron using the so-called "net function" (Eq. 6.1) to obtain the net input (u), and through the application of the net input into the so-called "activation function" (Eq. 6.2), to generate the output (y).

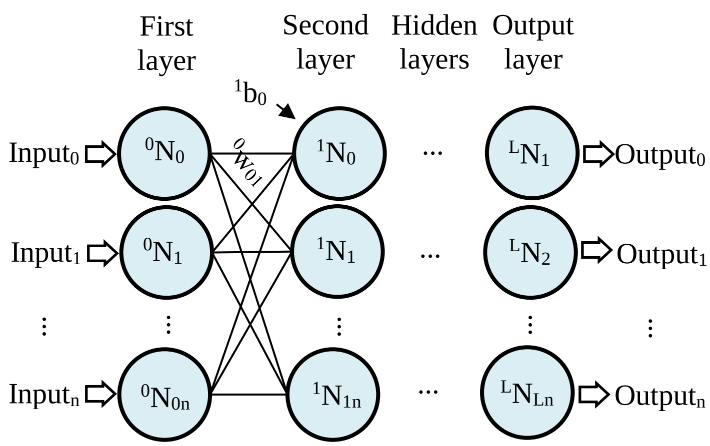

Figure 6-1: General structure of an artificial neural network.

Since the ANN is typically assigned random weights and biases, these outputs are generally inaccurate at first. To improve them, the ANN "learns" by calculating the error between its output predictions (O) and the desired output, called "target" (T) (Eq. 6.3), and using this error to modify the weights and biases in a process called "back propagation". After performing the back propagation, forward propagation is done again to reevaluate the ANN. This iterative procedure is repeated until the error in the ANN predictions is acceptably low, at which point the ANN is said to be trained.

After training, the ANN is typically tested with data that was never presented to it before. This has the purpose of ensuring that the network is able to generalize the results from the training to new scenarios, instead of only learning the specific cases experienced in the training. The testing is done by applying forward propagation and evaluating the error in the same manner as the training, with the difference that no backpropagation is performed and therefore the weights and biases are no longer updated. If the error in the predictions is acceptable at this stage, the ANN is said to be tested.

In this study, an artificial neural network is developed and used to predict the load capacity of adhesive anchors damaged by concrete cracking. To ensure that the ANN will have appropriate generalization ability after training a significant number of experimental results is needed to be used in the error evaluation. Furthermore, the specimens must have input parameters in a wide enough range since ANN predictions are not reliable outside the input range used during their training. For that end, data from a worldwide database kept by the ACI Committee 355 is obtained and used for training and testing of the network.

6.1 ANN Database Selection

The database contains experimental data from 2,929 adhesive anchors tested individually or in groups, under static or dynamic tension or shear loading, from 38 papers and reports from the USA, Europe, and Japan (Sakla and Ashour, 2005). To achieve this study's goal, only the specimens satisfying the following requirements are selected:

- Installation was done in cracked concrete.

- Boreholes were cleaned and dry.
- Loading application was short-term static tension.
- Anchors were tested individually.

This selection reduces the number of available specimens to 160, mainly because most tests are done in uncracked concrete. The range of each parameter in the selected specimens is presented in Table 6.1 and can be seen to cover typical anchor applications. To ensure that the ANN predictions have the most applicability, the training and testing sets (i.e. specimens used for training and testing, respectively) are carefully selected to cover each input parameter from its lowest to its highest values (Figure 6-2), as done by Sakla and Ashour (2005). The training set consists of 90% of the specimens (144 tests) and the remaining 10% (16 tests) are used as the testing set, a rate used by several researchers (e.g. Gesoglu and Guneyisi, 2007; Ashour and Alquedra, 2005; Sakla and Ashour, 2005).

Table 6.1**:** Types and range of parameters in the selected database.

Parameter	**Min**	**Max**	**Unit**
Anchor diameter	8	20	mm
Embedment Depth	80	170	mm
Annular gap	1.0	2.5	mm
Concrete strength	17.85	46.75	MPa
Crack width	0.00	0.55	mm
Load capacity	2.7	124.0	kN
Test method	Unconfined		
Loading type	Static		
Chemical system	Grout		
Adhesive type	Vynilester		
Bolt type	Threaded rod		
Cleaning	Clean, brushed, and dry		
Failure mode	Bolt, Concrete, B/M/C*		

*The database does not specify what the mode B/M/C means. It is assumed to mean “bond between bolt and mortar or mortar and concrete”.

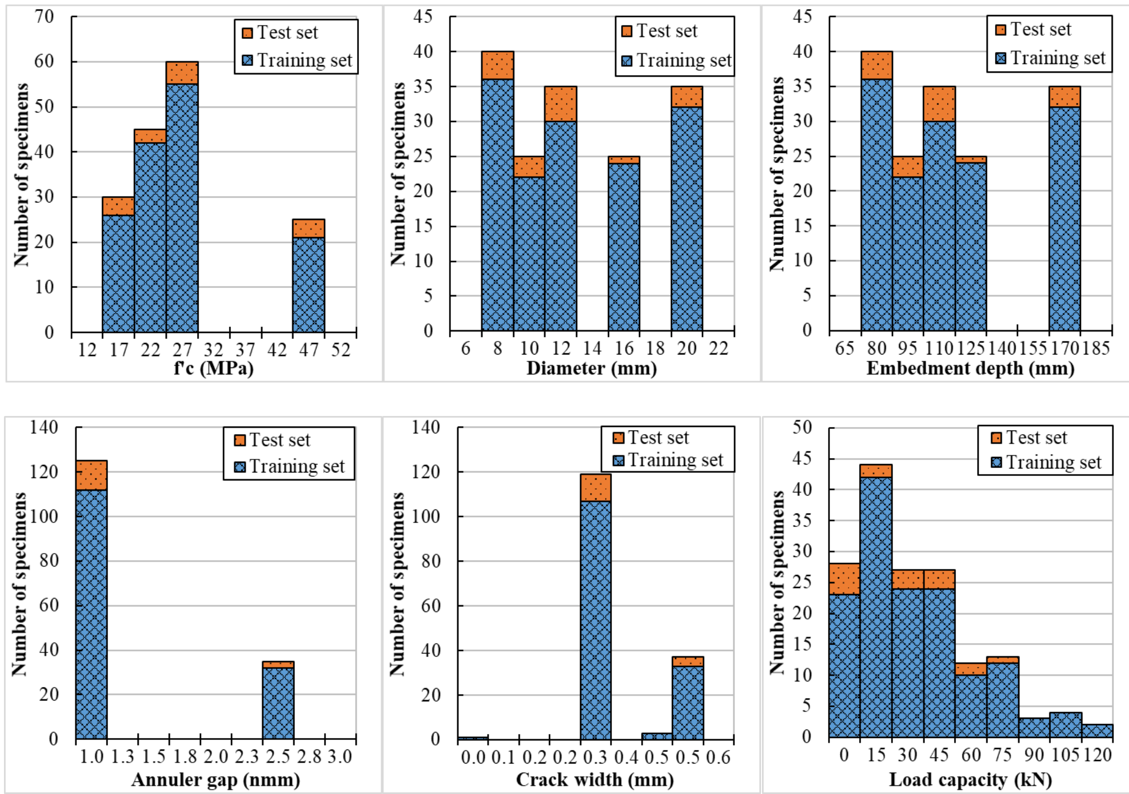

Figure 6-2: Distribution of parameters in the selected specimens.

6.2 ANN Development and Formulation

The neural network is developed using the multilayered feed-forward approach described above, as successfully done in the past. It is coded in the programming language C++ as it provides the necessary mathematical tools and computational efficiency desired. The input layer consists of five neurons receiving the variables: concrete compressive strength (f'_c), anchor diameter (d_a), anchor embedment depth (h_{ef}), annuler gap (A_g, i.e. space between the anchor and the borehole), and concrete crack width (w_{cr}). Only the variables presenting more than one value (Table 6.1) are included (i.e. factors such as the adhesive type were not considered given that only one type was present in the database).

The output layer (i.e. last layer) consists of one neuron to return the predicted load capacity of the adhesive anchor (*P*).

The net function consists of multiplying the input values by the weights and summing the bias to the result (Eq. 6.1), as commonly done (e.g. Gesoglu and Guneyisi, 2007; Ashour and Alquedra, 2005; Sakla and Ashour, 2005). The activation function chosen is the sigmoid function (Eq. 6.2) due to its desirable characteristics of accepting any input in the real domain and being smooth. This function has a higher slope for input near zero, which results in a faster convergence when inputs are close to zero. With that in mind, the inputs were normalized to the range [0, 1]. Due to the output image of the sigmoid, it is also necessary to convert the output back to the physical dominium.

$$^{L}x_i = \sum_{k=1}^{^{L-1}n} \left(^{L-1}w_{ki} \; ^{L-1}y_k \right) + {}^{L}b_i \qquad (6.1)$$

$$^{L}y_i = f\left(^{L}x_i = x \right) = \frac{1}{1+e^{-x}} \qquad (6.2)$$

Where:

$^{L}x_i$ = Input of neuron *i* in layer *L*

^{L-1}n = Number of neurons in layer *L-1*

$^{L-1}w_{ki}$ = Weight connecting neuron *k* in layer *L-1* to neuron *i* in layer *L*

$^{L-1}y_k$ = Output of neuron *k* in layer *L-1*

$^{L}b_i$ = Bias of neuron *i* in layer *L*

Backpropagation is performed by computing the total error (Eq. 6.3) and its derivatives with respect to each weight and bias (Eqs. 6.4 and 6.5), multiplying the result by a learning rate, and subtracting it from them according to Eqs. 6.6 and 6.7. The learning rate is a scalar between 0 and 1 used to reduce the rate of update of the weights and biases, which effectively prevents overfitting (Figure 6-3), ensuring that the ANN results can be generalized to never-seen data. However, selecting an excessively low learning rate results in slow training. In the present study, a learning rate of 0.5 is selected.

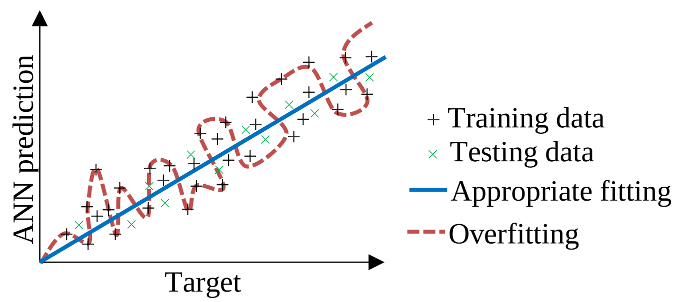

Figure 6-3: Example of appropriately fitted and overfitted curves.

$$E_{ANN} = \sum_{i=1}^{n_L} \frac{1}{2} \left[T_i - {}^{OL}y_i \right]^2 \quad (6.3)$$

$$\delta\, {}^{L}w_{ij} = \frac{\partial E}{\partial\, {}^{L}w_{ij}} \quad (6.4)$$

$$\delta\, {}^{L}b_i = \frac{\partial E}{\partial\, {}^{L}b_i} \quad (6.5)$$

$${}^{L}w_{ij} = {}^{L}w_{ij} - \eta . \delta\, {}^{L}w_{ij} \quad (6.6)$$

$${}^{L}b_i = {}^{L}b_i - \eta . \delta\, {}^{L}b_i \quad (6.7)$$

Where:

E_{ANN} = Total ANN error

T_i = Target of output neuron i

η = Learning rate

6.3 ANN Training and Testing

During the training, several iterations are performed by applying the forward propagation followed by backpropagation to each selected specimen. Various ANN configurations (i.e. number of neurons, number of layers, and input variables) including one and two hidden layers with two to six neurons are used and their total error and training time was recorded. The training error was observed to decrease with the number of neurons and hidden layers up to three neurons in the first hidden layer, when it reached a minimum (Figure 6-4). On the other hand, the training time increased almost linearly with the number of neurons (Figure 6-4).

The total number of iterations is varied from 10,000 – typically taken as the minimum number – to 500,000 to find the optimum value. Using an excessive number of iterations is avoided to prevent overfitting. The ANN accuracy was seen to increase asymptotically with the number of iterations (Figure 6-5a), while the training time increases in a nearly linear manner (Figure 6-5b). The optimum number of iterations was selected as 50,000, which provided satisfactory accuracy and training time (Figure 6-5c and 6-5d).

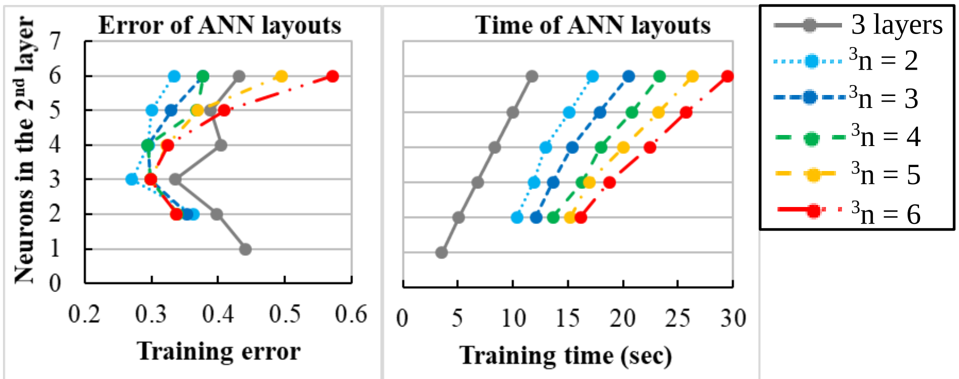

Figure 6-4: ANN training error and time for various configurations.

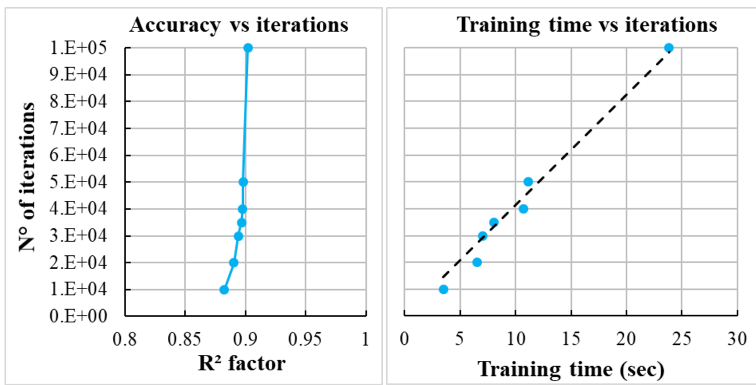

a) ANN accuracy b) ANN training time

Figure 6-5: ANN (a) accuracy and (b) training time vs the number of iterations.

After the training, testing of the ANN is performed by applying the forward propagation and computing the total error without updating the weights and biases. The testing of the 16 specimens was completed nearly instantaneously. The accuracy obtained in the testing predictions was higher than those from the training (Figure 6-7), confirming the generality of the ANN results to new specimens with parameters within the training range.

6.4 Final ANN Configuration

Based on the configurations studied, the optimum ANN configuration consisted of four layers with three neurons in the second and two in the third layers (Figure 6-6). Key parameters of this ANN include the use of the sigmoid as activation function, the number of training iterations, set to 50,000, and the learning rate selected as 0.5. Training of the ANN in this configuration takes approximately 12 seconds (Figure 6-4) and leads to accurate predictions of the anchor load capacity that are nearly equally above and below the experimental results, thus presenting no clear bias (Figure 6-7).

The ANN predictions after training are plotted versus the experimental capacities (i.e. targets) in Figure 6-7. The trendline that best fits this plot is defined by the equation $y = 1.02x$ and has an R^2 factor of 0.9, which is satisfactorily close to the ideal outcome of $y = 1.00x$ and $R^2 = 1$. Some deviation from the ideal line is observed in specimens with high capacity, which is mainly attributed to the low number of such specimens. Another factor may be that specimens installed in cracked concrete present a higher variability in load capacity when compared to specimens in uncracked concrete, which was noticed upon inspection of the database.

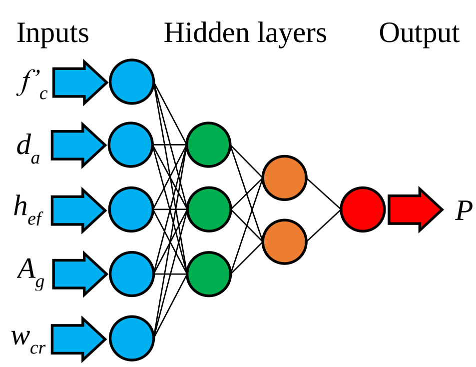

Figure 6-6: Optimum ANN configuration.

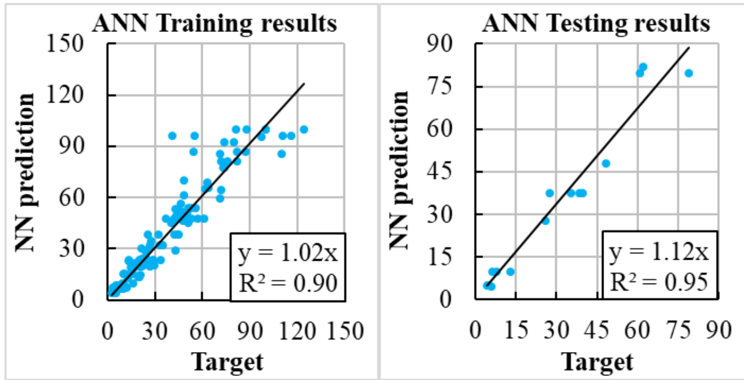

Figure 6-7: ANN training and testing results.

The trained and tested ANN was programmed in an open-access spreadsheet in a format readily available to be used by researchers and engineers to predict the capacity of adhesive anchors damaged by concrete cracking, which can be found at A. Almeida Jr. and Guner (2019a).

6.5 Influence of Key Input Parameters on the ANN Predictions

To test the sensitivity of the ANN to some of the key input parameters, a sensitivity study is performed. The ANN predictions are recorded for anchor embedment depths from 80 to 170 mm and anchor diameters from 8 to 20 mm. The results indicate that the load capacity of adhesive anchors damaged by concrete cracking varies linearly with the embedment depth in this range (Figure 6-8a), which agrees with the numerical sensitivity study performed for anchors in uncracked concrete. When the diameter was varied, the load capacity changed in a nonlinear way that can be approximated by two lines (Figure 6-8b) with the effect being more pronounced for larger diameters. This suggests that the relationship between bond failure capacity and anchor diameter in cracked concrete is different from the one in uncracked concrete. Further investigation is needed to confirm this relationship.

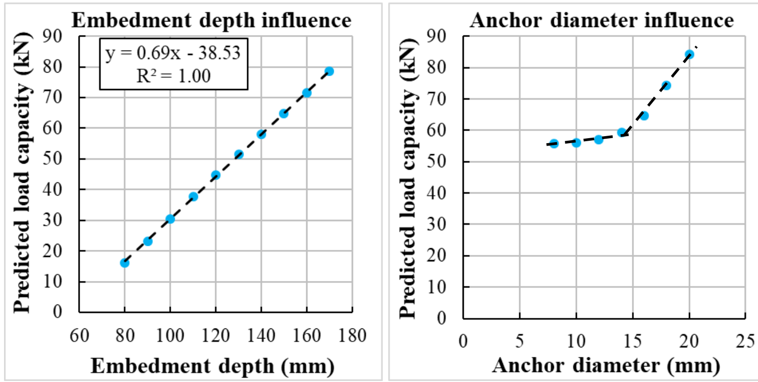

a) Embedment depth b) Anchor diameter

Figure 6-8: ANN Sensitivity to the anchor (a) embedment depth and (b) diameter.

Chapter 7

Conclusions

This study applied numerical modeling and artificial intelligence techniques to investigate and quantify the damage imposed on the anchorage of non-structural components (NSC) during hurricanes, which is caused by the bending of the NSC-supporting beams and the adverse environmental conditions to which the anchorage is exposed. For that purpose, 3D high-fidelity nonlinear finite element (FE) models ranging from single-anchors to holistic NSC-anchorage systems were created. The single-anchor models were verified with existing experimental data and used to quantify the damage caused on the anchors by adverse effects of elevated temperature and concrete cracking. They were also used to assess how key design parameters influence the anchor performance. Subsequently, the holistic NSC-anchorage models were used to investigate and quantify the damage caused by the bending of the NSC-supporting beams during hurricanes on the anchors. Based on the results, new design recommendations based on the geometry of the system were developed to mitigate this damage.

In addition, this study developed simpler and faster alternatives to facilitate the analysis of anchors. For that end, a novel 2D modeling approach named "equivalent cone" approach and an artificial neural network (ANN) were developed. The equivalent cone approach permits the anchor analyses to be performed using 2D models only, which are simpler to create, take less time to run, and are more computationally efficient. The approach was verified with the 3D numerical and existing experimental results and programmed into an open-access spreadsheet to be easily used by researchers and engineers. The developed ANN allows rapid prediction the load capacity of adhesive anchors damaged by concrete cracking with accuracy comparable to the FE models. It was trained and tested with experimental data from the worldwide database kept by ACI Committee 355 to provide the most applicability to its predictions. The influence of key input parameters on the ANN predictions was also assessed. The trained ANN was programmed into an open-access spreadsheet to be easily used by researchers and engineers to assess in the anchor design of analysis.

The following conclusions were drawn from the results of this study.

- 3D high-fidelity nonlinear FE anchor models were developed and successfully verified in the anchor failure modes of steel rupture in tension, concrete breakout, bond failure, and steel rupture in shear. The models predict the anchor load capacities with less than 10% error in all modes and capture the anchor load-displacement response accurately, except for a slight overestimation of the stiffness in some specimens presenting the concrete breakout mode.
- The 3D FE models were used to quantify the adverse effect of elevated temperature and concrete cracking, conditions typically present on rooftop slabs where NSC are anchored. Elevated temperature reduced the capacity by up to 70% in bond failure,

whereas the presence of concrete cracking reduced the anchor capacity by 20% in concrete breakout.

- The FE models were also used to assess the influence of the key design parameters on the single-anchor response, which was shown to depend on the anchor's failure mode. The steel rupture capacity in tension increases with the square of the anchor diameter and is insensitive to the embedment depth. The concrete breakout capacity is insensitive to the anchor diameter and increases with the embedment depth to the power 1.7, which is close to the 1.5 value used by ACI. In addition, it increases linearly with the concrete compressive and tensile strengths, the latter having a stronger influence. The bond failure capacity increases linearly with both the anchor diameter and embedment depth.
- Holistic analyses of an NSC-anchorage system were performed using the verified FE approach. During the analyses, the system failed under wind loading by tipping over in the direction of the wind, causing the two anchors in the leeward side to be pulled out in bond failure. The static lateral load capacity of the system is approximately the capacity of two anchors in tension. Under dynamic loading, the system failed at a slightly higher load capacity than under static wind loading but experienced significant accumulation of inelastic displacement.
- The holistic analyses showed that the bending of the NSC-supporting beams during hurricanes substantially damages the anchorage, promoting premature steel rupture of the anchor up to 62% below its design capacity. New design recommendations based on the geometry of the NSC-anchorage system were developed to mitigate this damage and therefore avoid this premature anchor failure.

- The developed equivalent cone approach permits the analysis of anchors to be performed using 2D FE models only, which are simpler to create and have reduced analysis time and computational expense. The approach was shown to achieve an accuracy in the anchor load capacity prediction similar to that of the 3D FE models.
- The developed artificial neural network rapidly and accurately predicts the load capacity of adhesive anchors damaged by concrete cracking. The ANN was trained and tested with experimental results from a worldwide database to provide the most applicability to its predictions and subsequently programmed on an open-access spreadsheet that can be easily used by researchers and engineers for the assessment of adhesive anchors damaged by concrete cracking.
- The time taken for ANN training increases in an almost linear fashion with the total number of neurons in the hidden layers and the number of iterations. In all cases, the ANN training time was of the order of seconds, much shorter than the time taken for the FE analysis of anchors, which was typically hours.
- The findings of this study regarding the damage caused on the anchors by the bending of the NSC-supporting beams during hurricanes and the adverse effects of elevated temperature and concrete cracking help to provide a more accurate assessment of the anchor capacity, therefore mitigating hurricane damage and resulting in significant savings in post-storm repair costs.

References

A. Almeida Jr, S. and Guner, S. (2019a) “Artificial neural network for adhesive anchors in cracked concrete”, Spreadsheet. <https://1drv.ms/x/s!ApwKeMnGrMg55e0T2TaHbbg8ETmgOQ>

A. Almeida Jr, S. and Guner, S. (2019b) “Equivalent cone approach”, Spreadsheet. <https://1drv.ms/x/s!ApwKeMnGrMg55eQRUVnu1UPuWCKmXg>

ABAQUS 6.14 (2014) “Analysis user’s guide” Vol. IV, Dassault Systèmes, Providence, Rhode Island, 1098 pp.

ACI Committee 318 (2014) “Building code requirements for structural concrete (ACI 318-14) and commentary” American Concrete Institute, Farmington Hills, MI. 519 pp.

American Society of Civil Engineers (ASCE) (2016) “Minimum design loads and associated criteria for buildings and other structures (ASCE/SEI 7-16)” American Society of Civil Engineers, Reston, VA. 822 pp.

Ashour, A. F. and Alqedra, M. A. (2005) “Prediction of shear capacity of single anchors located near a concrete edge using neural networks” Computer and Structures, 83: 2495–2502.

Çaliskan, Ö. and Aras, M. (2017) “Experimental investigation of behaviour and failure modes of chemical anchorages bonded to concrete” Construction and Building Materials, 156: 362–375.

Çaliskan, Ö, Yilmaz, S., Kaplan, H., and Kiraç, N. (2013) “Shear strength of epoxy anchors embedded into low strength concrete” Construction and Building Materials, 38: 723–730.

Cappucci, M. and Samenow, J. (2019) "'Bomb cyclone' bolts toward upper Midwest after blasting Colorado and the Plains" The Washington Post. Retrieved July 02, 2019, from <https://www.washingtonpost.com/weather/2019/03/14/bomb-cyclone-bolts-toward-upper-midwest-after-blasting-colorado-plains/?utm_term=.25992dbdd6b0>

Contrafatto, L. and Cosenza R. (2014) "Behaviour of post-installed adhesive anchors in natural stone" Construction and Building Materials, 68: 355–369.

Cook, R. A., Kunz, J., Fuchs, W., and Konz, R. C. (1998) "Behavior and design of single adhesive anchors under tensile loads in uncracked concrete" ACI Structural Journal, 95-S2: 9–26.

Cope, A. D. (2004) "Predicting the vulnerability of typical residential buildings to hurricane damage" Ph.D. Thesis. University of Florida, Florida, U.S.A., 222 pp.

U.S. Department of Homeland Security (2006) "Summary report on building performance" FEMA 548, 73 pp.

Cui, W. and Caracoglia, L. (2016) "Exploring hurricane wind speed along US Atlantic coast in warming climate and effects on predictions of structural damage and intervention costs" Engineering Structures, 122: 209–225.

Dinan, T. (2017) "Projected increases in hurricane damage in the United States: The role of climate change and coastal development" Ecological Economics, 138: 186–198.

Eligehausen, R., Bouska, P., Cervenka, V., and Pukl, R. (1992) "Size effect of concrete cone failure load on anchor bolts" Invited paper, 517–525.

Eligehausen, R., Cook, R., and Appl, J. (2006) "Behavior and design of adhesive bonded anchors" ACI Structural Journal, 103 (6): 822–832.

Emanuel, K. (2005) "Increasing destructiveness of tropical cyclones over the past 30 years" Nature, 436: 686–688.

Emanuel, K. A. (2013) “Downscaling CMIP5 climate models shows increased tropical cyclone activity over the 21st century” PNAS, 110(30): 12219–12224.

Epackachi, S., Esmaili, O., Mirghaderi, S. R., and Behbahani, A. A. T. (2015) “Behavior of adhesive bonded anchors under tension and shear loads” Journal of Constructional Steel Research, 114: 269–280.

Erwin, J. W., Chowdhury, A. G., and Bitsuamlak, G. (2011) “Wind load on rooftop equipment mounted on a flat roof” Journal of Wind and Engineering, 1: 23–42.

Fuchs, W., Hofmann, J., and Hulder G. (2016) “Effect of low-temperature installation on adhesive anchors” Concrete international: 48–56.

Gesoglu, M. and Güneyisi, E. (2007) “Prediction of load-carrying capacity of adhesive anchors by soft computing techniques” Materials and Structures, 40: 939–951.

Gesoglu, M., Güneyisi, E. M., Güneyisi, E., Yilmaz, M., E., and Mermerdas, K. (2014) “Modeling and analysis of the shear capacity of adhesive anchors post-installed into uncracked concrete” Composites: Part B, 60: 716–724.

Griffin, M. J. and Winn, V. (2009) “Nonstructural seismic performance for facilities in seismic regions: is the expected earthquake performance really bring achieved?” In ATC & SEI 2009 Conference on Improving the Seismic Performance of Existing Buildings and Other Structures, California, U.S.A., 11 pp.

Güneyisi, E. M., Gesoglu, M., Güneyisi, E., and Mermerdas, K. (2016) “Assessment of shear capacity of adhesive anchors for structures using neural network based model” Materials and Structures, 49: 1065–1077.

HILTI (2017) “North American product technical guide” Technical Guide, vol. 2, ed. 17, Plano, TX, U.S, 422 pp.

Hoehler, M. S., Mahrenholtz, P., and Eligehausen, R. (2011) “Behavior of anchors in concrete at seismic-relevant loading rates” ACI Structural Journal, 108-S24: 238–247.

Hosoya, N., Cermak, J. E., and Steele, C. (2001) “A wind-tunnel study of a cubic rooftop ac unit on a low building” In Americas Conference on Wind Engineering, South Carolina, U.S.A., 10 pp.

Kim J.-S., Jung W.-Y., Kwon M.-H., and Ju B.-S. (2013) “Performance evaluation of the post-installed anchor for sign structure in South Korea” Construction and Building Materials, 44: 496–506.

Knutson, T. R., Sirutis, J. J., Vecchi, G. A., Garner, S., Zhao, M., Kim, H.-S., Bender, M., Tuleya, R. E., Held, I. M. and Villarini, G. (2013) “Dynamical downscaling projections of twenty-first-century Atlantic hurricane activity: CMIP3 and CMIP5 model-based scenarios” American Meteorological Society, 26: 6591–6617.

Kossin, J. P., Knapp, K. R., Vimont, D. J., Murnane, R. J., and Harper, B. A. (2007) “A globally consistent reanalysis of hurricane variability and trends” Geophysical Research Letters, 34: 6pp.

Lahouar, M. A., Caron, J.-F., Foret, G., Benzarti, K., and Mege, R. (2018a) “Temperature effect on the mechanical behavior of glued-in rods intended for the connection of timber elements” Construction and Building Materials, 186: 438–453.

Lahouar, M. A., Caron, J.-F., Pinoteau, N., Forêt, G., and Benzarti, K. (2017) “Mechanical behavior of adhesive anchors under high temperature exposure: experimental investigation” International Journal of Adhesion and Adhesives, 78: 200–211.

Lahouar, M. A., Pinoteau, N., Caron, J.-F., Foret, G., and Mege, R. (2018b) “A nonlinear shear-lag model applied to chemical anchors subjected to a temperature distribution” International Journal of Adhesion and Adhesives, 84: 438–450.

Lahouar, M. A., Pinoteau, N., Caron, J.-F., Foret, G., and Rivillon, P. (2018c) “Fire design of post-installed bonded rebars: full-scale validation test on a 2.94 x 2 x 0.15 m^3 concrete slab subjected to ISO 834-1 fire” Engineering Structures, 174: 81–94.

Mahrenholtz, P., Eligehausen, R., and Hutchinson, T. C. (2014) “Seismic displacement behavior of anchors connecting non-structural components to cycling cracked concrete”

In Second European Conference on Earthquake Engineering and Seismology, Istanbul, Turkey, 12 pp.

Mahrenholtz, C., Eligehausen, R., Hutchinson, T. C., and Hoehler, M. S. (2017) “Behavior of post-installed anchors tested by stepwise increasing cyclic crack protocols” ACI Structural Journal, 114-S50: 621–630.

Mahrenholtz, P., Hutchinson, T. C., and Eligehausen, R. (2016) “Performance of suspended nonstructural components and their anchorage during shake table tests” Earthquake Spectra, 32(3): 1325-1343.

Mahrenholtz, P., Hutchinson, T. C., and Eligehausen, R. (2014) “Shake table tests on suspended non-structural components anchored in cyclically cracked concrete” Journal of Structural Engineering, 140 (11).

Marcon, M., Vorel, J., Nincević, K., and Wan-Wendner, R. (2017) “Modeling adhesive anchors in a discrete element framework” Materials, 10, 917: 1–23.

Masoomi, H., van de Lindt, J. W., Ameri, M. R., Do, T. Q., and Webb, B. M. (2018) “Combined wind-wave-surge hurricane-induced damage prediction for buildings” Journal of Structural Engineering, 145(1): 1 - 15.

McVay, M., Cook, R. A., and Krishnamurthy, K. (1996) “Pullout simulation of postinstalled chemically bonded anchors” Journal of Structural Engineering, 1016–1024.

Mohyeddin, A., Gad, E. F., Yangdon, K., Khandu, R., and Lee, J. (2016) “Tensile load capacity of screw anchors in early age concrete” Construction and Building Materials, 127: 702–711.

Mudd, L., Wang, Y., Letchford, C., and Rosowsky, D. (2014) “Assessing climate change impact on the U.S. east coast hurricane hazard: temperature, frequency and track” Natural Hazards Review, 04014001.

Nilforoush, R., Nilsson, M., and Elfgren, L. (2017) “Experimental evaluation of tensile behaviour of single cast-in-place anchor bolts in plain and steel fibre-reinforced normal- and high-strength concrete” Engineering Structures, 147: 195–206.

Nilforoush, R., Nilsson, M., Söderlind, G., and Elfgren, L. (2016) “Long-term performance of adhesive bonded anchors” ACI Structural Journal, 113-S23: 251–261.

NOAA (2017) “Extremely active 2017 Atlantic hurricane season finally ends” National Oceanic and Atmospheric Administration (NOAA). Retrieved July 02, 2019, from <https://www.noaa.gov/media-release/extremely-active-2017-atlantic-hurricane-season-finally-ends>

NOAA (2019) “U.S. billion-dollar weather and climate disasters” NOAA National Centers for Environmental Information (NCEI). Retrieved April 26, 2019, from <https://www.ncdc.noaa.gov/billions/summary-stats>

Sakla, S. S. S. and Ashour, A. F. (2005) “Prediction of tensile capacity of single adhesive anchors using neural networks” Computers and Structures, 83: 1792–1803.

Sato, H., Fujikake, K., and Mindess, S. (2004) “Study on dynamic pullout strength of anchors based on failure modes” In 13th World Conference on Earthquake Engineering, Vancouver, Canada, 7 pp.

Sharma, A., Eligehausen, R., and Asmus, J. (2017) “Experimental investigation of concrete edge failure of multiple-row anchorages with supplementary reinforcement” Structural Concrete, Journal of fib, 18(1): 153–163.

Simon, J. (2017) “A lonely aerial view of Irma’s destruction in the Florida Keys” Quartz. Retrieved July 03, 2019, from <https://qz.com/1078828/hurricane-irma-damage-an-aerial-view-of-the-destruction-irma-left-behind-in-the-florida-keys/>

Solomos, G. and Berra, M. (2006) “Testing of anchorages in concrete under dynamic tensile loading” Materials and Structures, 39: 695–706.

Thurston, C. (2015) “Ensuring your solar array doesn’t get caught in the wind” Renewable Energy World. Retrieved July 03, 2019, from <https://www.renewableenergyworld.com/articles/print/volume-18/issue-4/features/solar/ensuring-your-solar-array-doesn-t-get-caught-in-the-wind.html>

Tsavdaridis, K. D., Shaheen, M. A., Baniotopoulos, C., and Salem, E. (2016) "Analytical approach of anchor rod stiffness and steel base plate calculation under tension" Structures, 5: 207–218.

U.S. Department of Homeland Security (2018) "Attachment of rooftop equipment in high-wind regions" FEMA, 8 pp.

U.S. Department of Homeland Security (2006) "Summary report on building performance" FEMA 548, 73 pp.

Villarini, G. and Vecchi, G. A. (2012) "Twenty-first-century projections of North Atlantic tropical storms from CMIP5 models" Nature Climate Change, 2: 604–607.

Wahalathantri, B. L., Thambiratnam, D. P., Chan, T. H. T., and Fawzia, S. (2011) "A material model for flexural crack simulation in reinforced concrete elements using Abaqus" In Proceedings of the First International Conference on Engineering, Designing and Developing the Built Environment for Sustainable Wellbeing, Brisbane, Australia, 5 pp.

Wang, D., Wu, D., Ouyang, C., He, S., and Sun, X. (2017) "Simulation analysis of large-diameter post-installed anchors in concrete" Construction and Building Materials, 143: 558–565.

Webster, P. J., Holland, G. J., Curry, J. A., and Chang H.-R. (2005) "Changes in tropical cyclone number, duration, and intensity in a warming environment" Science, 309: 1844–1846.

Wong, P. S., Vecchio, F. J., and Trommels H. (2002) "VecTor2 & formworks user's manual" 2nd ed., 318 pp.